JACS
JOURNAL OF THE AMERICAN CHEMICAL SOCIETY

ARTICLE

pubs.acs.org/JACS

Water Oxidation by a Mononuclear Ruthenium Catalyst: Characterization of the Intermediates

Dmitry E. Polyansky,*[,†] James T. Muckerman,[†] Jonathan Rochford,[†,§] Ruifa Zong,[‡] Randolph P. Thummel,[‡] and Etsuko Fujita*[,†]

[†]Chemistry Department, Brookhaven National Laboratory, Upton, New York 11973-5000, United States

[‡]Department of Chemistry, University of Houston, Houston Texas 77204-5003, United States

Supporting Information

ABSTRACT: A detailed characterization of intermediates in water oxidation catalyzed by a mononuclear Ru polypyridyl complex $[\mathbf{Ru}^{II}-OH_2]^{2+}$ (**Ru** = Ru complex with one 4-*t*-butyl-2,6-di-(1′,8′-naphthyrid-2′-yl)-pyridine ligand and two 4-picoline ligands) has been carried out using electrochemistry, UV−vis and resonance Raman spectroscopy, pulse radiolysis, stopped flow, and electrospray ionization mass spectrometry (ESI-MS) with $H_2{}^{18}O$ labeling experiments and theoretical calculations. The results reveal a number of intriguing properties of intermediates such as $[\mathbf{Ru}^{IV}{=}O]^{2+}$ and $[\mathbf{Ru}^{IV}-OO]^{2+}$. At pH > 2.9, two consecutive proton-coupled one-electron steps take place at the potential of the $[\mathbf{Ru}^{III}-OH]^{2+}/[\mathbf{Ru}^{II}-OH_2]^{2+}$ couple, which is equal to or higher than the potential of the $[\mathbf{Ru}^{IV}{=}O]^{2+}/[\mathbf{Ru}^{III}-OH]^{2+}$ couple (i.e., the observation of a two-electron oxidation in cyclic voltammetry). At pH 1, the rate constant of the first one-electron oxidation by Ce(IV) is $k_1 = 2 \times 10^4\ M^{-1}\ s^{-1}$. While pH-independent oxidation of $[\mathbf{Ru}^{IV}{=}O]^{2+}$ takes place at 1420 mV vs NHE, bulk electrolysis of $[\mathbf{Ru}^{II}-OH_2]^{2+}$ at 1260 mV vs NHE at pH 1 (0.1 M triflic acid) and 1150 mV at pH 6 (10 mM sodium phosphate) yielded a red colored solution with a Coulomb count corresponding to a *net four-electron oxidation.* ESI-MS with labeling experiments clearly indicates that this species has an O−O bond. This species required an additional oxidation to liberate an oxygen molecule, and without any additional oxidant it completely decomposed slowly to form $[\mathbf{Ru}^{II}-OOH]^{+}$ over 2 weeks. While there remains some conflicting evidence, we have assigned this species as $^1[\mathbf{Ru}^{IV}-\eta^2\text{-}OO]^{2+}$ based on our electrochemical, spectroscopic, and theoretical observations alongside a previously reported analysis by T. J. Meyer's group (*J. Am. Chem. Soc.* **2010**, *132*, 1545−1557).

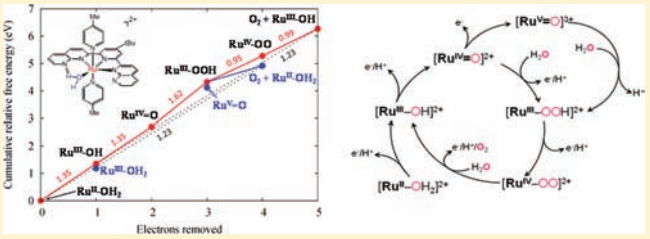

INTRODUCTION

Artificial photosynthesis holds the promise of providing solar fuels from water powered by sunlight.[1−12] Considerable progress has been made in the development of oxidation catalysts that might serve as one component of such a solar conversion system.[13−46] Many of these catalysts are based on ruthenium polypyridyl complexes, and most of these complexes can be roughly categorized as dinuclear[15,17−26] or mononuclear[28−34] catalysts. Initially, it was thought that two adjacent metal centers would be needed to enable the eventual formation of the critical O−O bond. More recently, it has been discovered that dioxygen can be produced by the nucleophilic interaction of a water molecule with a single Ru=O center such as $[Ru(tpy)(bpy)(O)]^{3+}$ and $[Ru(tpy)(bpm)(O)]^{3+}$ (tpy = 2,2′:6′,2″-terpyridine, bpy = 2,2′-bipyridine, bpm = 2,2′-bipyrimidine), and this finding has generated some interesting mechanistic interpretations.

In one type of mononuclear Ru catalyst, a tetradentate ligand occupies the equatorial plane of the molecule, and two monodentate pyridines occupy the axial sites.[25,28,45−47] The pyridines do not exchange with a water (solvent) molecule, prompting Thummel and co-workers to propose a mechanism that involves two initial one-electron oxidations to produce a 6-coordinate, 16-electron Ru^{IV} species that subsequently undergoes attack by water at the metal center to expand the coordination shell to seven.[29] Sun and co-workers have structurally characterized a similar 7-coordinate intermediate as a dimeric species for a system in which the equatorial ligand is 6,6′-dicarboxy-2,2′-bipyridine.[25,46] The other class of mononuclear Ru catalyst has water bound to the metal in the resting state of the catalyst. Initial oxidation of the catalyst by a sacrificial oxidant such as Ce(IV) results in the loss of two electrons accompanied by the loss of two protons to produce a Ru(IV) oxo species. Proton-coupled electron transfer (PCET) reactions for the oxidation of $[Ru(tpy)(bpy)(OH_2)]^{2+}$ to $[Ru(tpy)(bpy)(O)]^{2+}$ were investigated as early as 1984,[48] but their relevance to catalytic activity for water oxidation was only recently recognized.[32] Meyer[30,34,49−51] and Berlinguette[35,36] have elegantly investigated the kinetics and mechanisms of water oxidation with their $[Ru(NNN)(NN)(OH_2)]^{2+}$ catalysts (NNN = tpy or tpy-like molecule such as 2,6-bis(benzimidazol-2′-yl)pyridine, NN = bpm, bpy, 4,4′-$(HOOC)_2$bpy, and 4,4′-$(MeO)_2$bpy). The major pathway seems to proceed through a $[\mathbf{Ru}^{IV}{=}O]^{2+}$ species produced by proton-coupled electron transfer (PCET)

Received: April 8, 2011
Published: August 04, 2011

Chart 1. Structure of $[Ru^{II}-OH_2]^{2+}$

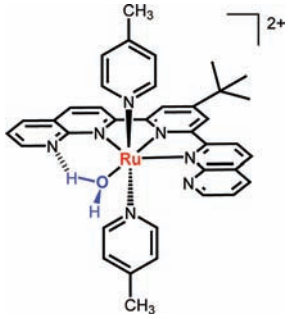

reactions, which is further oxidized to $[Ru^{V}=O]^{3+}$, a key intermediate that reacts with water to produce an O−O bond. Both groups proposed possible competing reaction pathways that involve $[Ru^{IV}-OO]^{2+}$, $[Ru^{V}-OO]^{3+}$, and $[Ru^{II}-O_2H_2]^{2+}$ intermediate species, and Berlinguette[35,36] proposed additional pathways via disproportionation of $[Ru^{IV}=O]^{2+}$ and the oxidative addition of $[Ce^{IV}(NO_3)_5]^{-}$ to $[Ru^{IV}=O]^{2+}$ to form $[Ru^{IV}-OO]^{2+}$. While the $Ru^{V}=O/Ru^{IV}=O$ potentials of these Ru centers (1.77−1.89 V) are close to the thermodynamic limit of oxidation by Ce(IV) (the Ce^{IV}/Ce^{III} potential is 1.61 V in 1.0 M HNO_3), the addition of 1 equiv of Ce(IV) to $[Ru^{IV}=O]^{2+}$ is proposed to generate $[Ru^{V}=O]^{3+}$, which, in turn, undergoes O−O bond formation. However, spectroscopic, electronic, and geometric characterization of these Ru−OO, Ru−OOH, and $Ru-O_2H_2$ species remains unclear.

In the current study, we examine the complex $[\mathbf{Ru}^{II}-OH_2]^{2+}$ (**Ru** = Ru(NPM)(pic)$_2$, NPM = 4-*t*-butyl-2,6-di-(1′,8′-naphthyrid-2′-yl)-pyridine, pic = 4-picoline, Chart 1), which is one of the first reported Ru-based mononuclear water oxidation catalysts.[28] Unlike the $[Ru(tpy)(NN)(H_2O)]^{2+}$ (where NN represents 2,2′-bipyridine and its derivatives) species mentioned above, in this catalyst the water molecule occupies a fourth binding site in the equatorial plane. The X-ray single-crystal structure shows that the coordinated water molecule is H-bonded to a noncoordinated nitrogen on one of the two 1,8-naphthyridyl rings appended to the central pyridine.[28] The complex has two axial picolines and in that respect resembles the first type of catalyst having a tetradentate equatorial ligand. The presence of an internal basic site may make this complex well suited for proton-coupled electron transfer events.

Here we present experimental results on the one- and two-electron oxidized species, the pathways of their formation, their electronic structures, and their reactivities and discuss the mechanism of water oxidation catalyzed by $[\mathbf{Ru}^{II}-OH_2]^{2+}$ based on collective observations from electrochemistry, UV−vis and resonance Raman spectroscopy, pulse radiolysis, stopped flow, ESI-MS, $H_2{}^{18}O$ labeling experiments, and theoretical calculations. The most intriguing result is the electrochemical formation of $[\mathbf{Ru}^{IV}-OO]^{2+}$ observed with a Coulomb count corresponding to a *net four-electron oxidation* when 1260 mV vs NHE at pH 1 or 1150 mV at pH 6 was applied to a solution containing $[\mathbf{Ru}^{II}-OH_2]^{2+}$, despite the fact that the $\mathbf{Ru}^{V}=O/\mathbf{Ru}^{IV}=O$ potential is 1420 mV. (NB: We use the formal oxidation state of "IV" for the O−O bonded species in accordance with the convention employed in various previous publications on water oxidation with Ru complexes; however, it could be a species between $[\mathbf{Ru}^{IV}-OO]^{2+}$ and $[\mathbf{Ru}^{III}-(OO^{-\bullet})]^{2+}$) The red colored species produced by this electrolysis requires 1 equiv of oxidant to produce O_2. Without the oxidant, the species slowly decomposes over two weeks to form $[\mathbf{Ru}^{II}-OOH]^{+}$ that is identified by ESI-MS and other spectroscopic techniques.

EXPERIMENTAL SECTION

Materials. The complex $[\mathbf{Ru}^{II}-OH_2]^{2+}$ was prepared as described previously.[28] All chemicals used were 99% grade or higher and used without further purification, except for the following. Trifluoromethanesulfonic acid was ReagentPlus grade (Aldrich), distilled under vacuum and immediately used to prepare a 1.0 M aqueous stock solution. The solution was stored under refrigeration (ca. 10 °C). Ceric ammonium nitrate was dried under vacuum and used to prepare acidic (triflic acid) solutions. Ceric solutions were titrated with a known concentration of sodium oxalate to determine accurate concentrations of the ceric ion. Aqueous solutions were prepared with distilled water that had been passed through a Millipore ultrapurification system. Blanket gases (N_2O, Ar) were UHP grade (99.999%).

Spectroscopic Measurements. UV−vis spectra were measured on a Hewlett-Packard 8452A diode-array spectrophotometer or Varian Cary 500 dual-beam spectrometer. NMR spectra were measured on a Bruker UltraShield 400 MHz spectrometer. Gas analysis was performed with a QMS 100 residual gas analyzer (Stanford Research). An Applied Photophysics stopped-flow system configured for two-syringe mixing was used to carry out stopped flow experiments. Spectral changes were detected with a PDA detector in the 300−800 nm range. Single wavelength kinetic traces were recorded using a PMT detector. In a typical experiment, one syringe was charged with an excess of Ce(IV) solution in 0.2 M triflic acid, and the other syringe contained a solution of the ruthenium complex in water. The spectral change was recorded after equal amounts of both solutions were mixed in a 1 cm stopped-flow cell. The dead time of the mixing setup was 2 ms.

Resonance Raman spectroscopy. Resonance Raman spectra were measured using focused output (1 mm) of the second harmonic of a YAG:Nd^{3+} laser (532 nm; Continuum, Powerlite 7010, 10 ns, 2 Hz, 20 mJ/pulse). The front-scattered light was collected by a 100 mm achromatic lens and collimated to a 200 mm achromatic lens. The second lens was f-matched with the SpectraPro 300i spectrograph (Acton) equipped with a liquid nitrogen cooled Spec-10 CCD (Acton). A long pass filter (RazorEdge LP03-532 from Semrock) was placed in front of the spectrograph entrance slits to eliminate stray light from the laser excitation. The spectrograph and CCD control as well as spectral acquisition was archived with WinSpec software (Acton). The spectra were recorded at CCD temperature of −100 °C and corrected for background noise and cosmic ray hits. The spectrograph was calibrated using known Raman shift values for the acetonitrile/toluene mixture. The calibration was performed before and after each measurement using an external standard, and the deviation between two measurements was found to be always less than 1 cm^{-1}. The sample for Raman measurements was prepared by electrolyzing ca. 0.3−0.4 mM aqueous solutions of $[\mathbf{Ru}^{II}-OH_2]^{2+}$ and subsequent concentration of these solutions to ca. 1.5−2 mM under vacuum. The resulting concentrated solutions were placed into a syringe which was connected to a PEEK capillary tube. The end of the capillary was mounted in the focal plane of the 100 mm collection lens, and a drop of liquid was carefully expelled from the end of the capillary. The capillary was aligned using an X−Y translation stage in such way that the focused laser beam was going through the hanging drop of liquid. A typical spectrum was recorded using 10 s accumulation time and 16 averages, followed by replacement of the drop with the fresh sample. The data postprocessing included the averaging of at least 8 spectra followed by a baseline correction. The use of the hanging drop technique allowed recording Raman spectra unobstructed by intense Raman lines originated from a cell material. UV−vis spectra taken before and after Raman experiments showed no significant decomposition of the sample due to exposure to the laser radiation.

Electrochemical Measurements. All potentials are reported vs NHE. Electrochemical measurements of redox reactions of $[\mathbf{Ru}^{II}-OH_2]^{2+}$ were conducted with a BAS 100b electrochemical analyzer from Bioanalytical Systems. Cyclic voltammograms and square wave voltammograms in aqueous solutions were measured using 0.5 mM solutions of

$[\mathbf{Ru}^{II}-OH_2]^{2+}$ in water containing 20% 2,2,2-trifluoroethanol, 0.1 M sodium trifluoromethanesulfonate, and 10 mM sodium phosphate (in the 2−10 pH range) or 0.1 M trifluoromethanesulfonic acid (at pH 1). In contrast to acetonitrile, trifluoroethanol does not exchange with water in the ruthenium coordination sphere but still enhances the solubility of $[\mathbf{Ru}^{II}-OH_2]^{2+}$. A glassy carbon disk was used as a working electrode, a platinum wire as a counter electrode, and Ag/AgCl (sat. NaCl) as a reference electrode. For measurements in acetonitrile, 0.1 M $[(t\text{-}Bu)_4N][PF_6]$ was used as an electrolyte, and a nonaqueous $Ag/AgNO_3$ electrode was used as a reference (potentials converted to NHE using an external Fc^+/Fc standard (640 mV vs NHE[52]). The scan rate in all CV experiments was 100 mV s^{-1} unless noted otherwise. In bulk electrolysis experiments, glassy carbon was replaced with a platinum gauze electrode, and the platinum counter electrode was isolated with a Vycor frit.

Pulse Radiolysis. Pulse radiolysis studies were carried out using the BNL 2 MeV van de Graaff accelerator using electron pulses (pulse width of 40−500 ns) that led to irradiation doses of 10−1000 rad (ca. 0.5−5 μM primary radicals) generated in solution. A thiocyanate solution (0.01 M KSCN, 0.026 M N_2O) was used for dosimetry taking $G((SCN)_2^-)$ = 6.13 (G = number of species formed per 100 eV of energy absorbed by the solution) and $\varepsilon_{472nm} = (7590 \pm 230)$. The optical path of the cell was 2 cm. All measurements were carried out in aqueous solutions containing 10 mM $NaHCO_3/Na_2CO_3$ at pH 10 saturated with N_2O at 25 °C. Under these conditions, the conversion of the primary radicals to the carbonate radical was complete by the first microsecond. Quoted rate constants have an error of ca. 15%. All rates measured in the pulse radiolysis studies are averages of at least three measurements. The pH of the solution was adjusted by addition of sodium hydroxide or trifluoromethanesulfonic acid.

Oxygen Measurements. Gases produced during catalytic water oxidation were analyzed with a QMS 300 Gas Analyzer (Stanford Research Systems). The headspace of the reaction vessel was connected to a capillary, leading to the inlet of the gas analyzer. The reaction vessel was connected to the argon supply line to maintain constant pressure inside the vessel. Deaerated ceric solutions were injected into the deaerated catalyst solution through a septum. The analyzer was set up to monitor m/z signals which corresponded to oxygen, nitrogen, and carbon dioxide. In experiments with isotopically labeled water, an 85% enrichment of ^{18}O was used.

Electronic Structure Calculations. All calculations were performed with the Gaussian 09 program package,[53] and all DFT calculations were carried out using the B3LYP hybrid functional.[54−58] We employed the B3LYP/ECP28MWB(1f,0 g)[Ru];[59,60] 6-311G(d,p)[H,C,N,O][61,62]// B3LYP/ECP28MWB(1f,0g)[Ru]; 6-31G(d)[O,N]; 6-31G[H,C] method.[63−68] The ECP28MWB(1f,0g) is a triple-ζ plus polarization and diffuse functions basis, (8s7p6d1f)/[6s5p3d1f], for Ru that is common to the small and large basis sets. The 6-31G(d)[O,N]; 6-31G[H,C] small basis for the nonmetal atoms is a double-ζ plus polarization basis for O and N and double-ζ for C and H.[64] The large basis for the nonmetal atoms is a triple-ζ plus polarization basis for H, C, N, and O. For the case of $[\mathbf{Ru}^{II}-OH_2]^{2+}$, the small basis has 580 functions, and the large basis has 1105 functions.

For all species considered in the proposed catalytic water oxidation cycle, a single explicit solvent water molecule was included in the calculation to provide hydrogen bonding to the water species bound to the metal center. The effect of the bulk solvent was included in all geometry optimization and vibrational frequency calculations of species with standard states in solution through the use of the C-PCM method[69−71] using UAKS radii. The absolute standard Gibbs free energy in aqueous solution (or in the gas phase for H_2 and O_2), along with appropriate values of the absolute free energy of the solvated proton and gas-phase electron, were used to calculate standard free energy changes of reaction and standard reduction potentials (see "Details of Electrochemistry in Aqueous Solution" in Supporting Information). The reduction potentials were referenced to a value for the absolute potential of the normal hydrogen electrode (NHE) obtained using the experimental absolute free energies of H_2 and an electron in the gas phase together with the experimental value of the absolute free energy of the solvated proton in water. Representative thermodynamic cycles are provided in Schemes S1−S3 (Supporting Information). Additional TD-B3LYP calculations were carried out for selected species to aid in their identification from UV−vis spectra in electrochemical and pulse radiolysis experiments.

In cases in which there was a question of whether the ground electronic state of a species is a singlet or a triplet, three kinds of additional calculations were carried out. Each of these additional methods goes beyond standard density functional theory in treating multiconfigurational effects. The first of these was a broken symmetry (BS) B3LYP calculation to see if there was a singlet state with antiferromagnetically coupled unpaired electrons with lower energy than the closed-shell singlet. The second was a CASSCF calculation of both the singlet and triplet species. The CASSCF calculation explored the possibility of there being important valence configurations, e.g., GVB-CI electron pairs, not accounted for by the single-configuration B3LYP method. The third was a multireference MP2 calculation on the $[\mathbf{Ru}^{IV}{=}O]^{2+}$ species based on the CASSCF wave function that includes the effect of dynamic correlation in addition to the static valence correlation in the reference function.

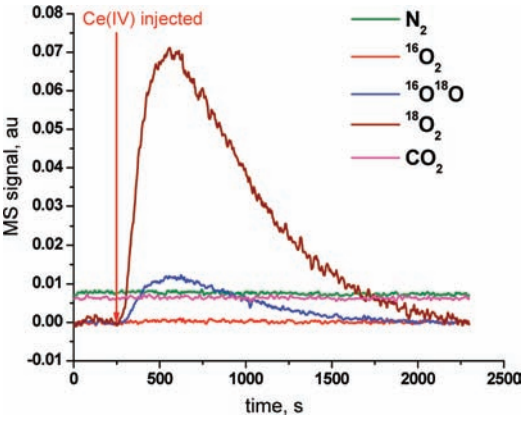

Figure 1. Gas evolution analysis during chemical (Ce(IV) in triflic acid, pH 1) oxidation of $[Ru^{II}-OH_2]^{2+}$ (50 μM) in $H_2{}^{18}O$. The amount of Ce(IV) relative to the catalyst was 80 equivalents.

RESULTS

Evidence for Catalytic Water Oxidation Mediated by $[\mathbf{Ru}^{II}-OH_2]^{2+}$. Catalytic performance of water oxidation catalysts is typically evaluated by analyzing catalytic current during the electrochemically driven oxidation reaction or by utilizing Ce(IV) salts such as ceric ammonium nitrate as a sacrificial oxidant. While ceric salts are very potent oxidation reagents (the $E°$ of Ce^{IV}/Ce^{III} is 1.3−1.9 V vs NHE),[72] the potential of the Ce^{IV}/Ce^{III} couple is strongly dependent on the nature of the acid and its concentration.[72−75]

As was previously reported, the presence of catalytic amounts of $[\mathbf{Ru}^{II}-OH_2]^{2+}$ in an acidic solution of Ce(IV) leads to oxygen formation with TN = 260[28,29] as determined by monitoring the formation of O_2 gas. In the current study, the analysis of the gaseous products was extended to include not only oxygen and its isotopes but also other gases (Figure 1). The absence of measurable amounts of carbon dioxide indicates that decomposition of $[\mathbf{Ru}^{II}-OH_2]^{2+}$ involving oxidation of the organic ligands does not take place under the reaction conditions (ca. 20 TN). CO_2 evolution

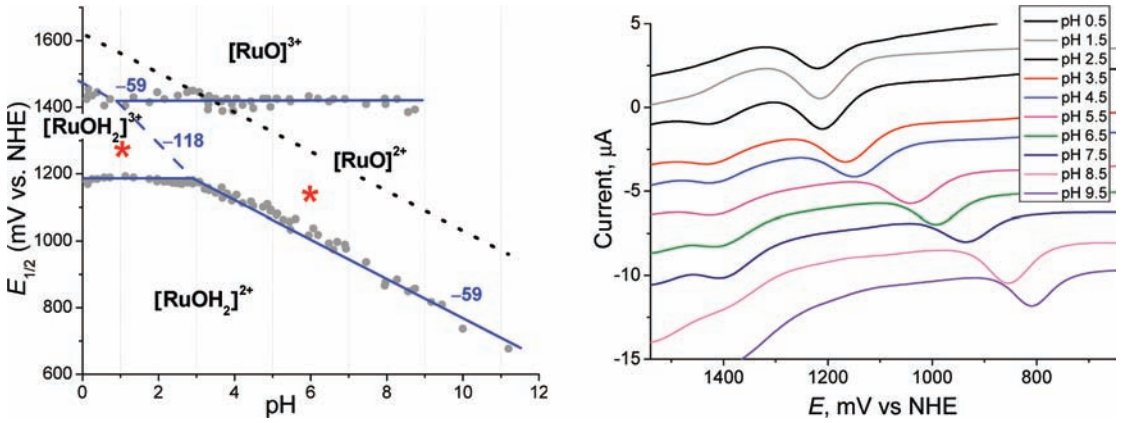

Figure 2. pH-dependent electrochemistry of $[\mathbf{Ru}^{II}-OH_2]^{2+}$: Pourbaix diagram (left). The dotted line corresponds to the calculated potential for $[\mathbf{Ru}^{IV}=O]^{2+} + H_2O - e^- \rightarrow [\mathbf{Ru}^{III}-OOH]^{2+} + H^+$, and the red stars indicate the conditions of bulk electrolysis experiments. Square wave voltammograms recorded in the pH range 0.5−9.5 (right).

has been previously observed as a result of ruthenium polypyridyl complex oxidation and was attributed to ligand decomposition.[13]

Electrochemistry of $[Ru^{II}-OH_2]^{2+}$. During electrochemical oxidation of $[\mathbf{Ru}^{II}-OH_2]^{2+}$ in aqueous acidic solution (pH 1), the catalytic current started to develop above ca. 1500 mV and increased as the concentration of $[\mathbf{Ru}^{II}-OH_2]^{2+}$ increased as shown in Figure S1 (Supporting Information).

$$[\mathbf{Ru}^{II}-OH_2]^{2+} - e^- - H^+ \rightarrow [\mathbf{Ru}^{III}-OH]^{2+} \quad (1)$$

$$[\mathbf{Ru}^{III}-OH]^{2+} - e^- - H^+ \rightarrow [\mathbf{Ru}^{IV}=O]^{2+} \quad (2)$$

$$[\mathbf{Ru}^{II}-OH_2]^{2+} - e^- \rightarrow [\mathbf{Ru}^{III}-OH_2]^{3+} \quad (3)$$

$$[\mathbf{Ru}^{III}-OH_2]^{3+} - e^- - 2H^+ \rightarrow [\mathbf{Ru}^{IV}=O]^{2+} \quad (4a)$$

$$[\mathbf{Ru}^{III}-OH_2]^{3+} - 2e^- - 2H^+ \rightarrow [\mathbf{Ru}^{V}=O]^{3+} \quad (4b)$$

$$[\mathbf{Ru}^{IV}=O]^{2+} - e^- \rightarrow [\mathbf{Ru}^{V}=O]^{3+} \quad (5)$$

The pH dependence of the electrochemical oxidation of $[\mathbf{Ru}^{II}-OH_2]^{2+}$ in aqueous solution is summarized in Figure 2 and eqs 1−5. Ru−aqua polypyridyl complexes such as $[Ru(tpy)(bpy)(OH_2)]^{2+}$ are known to lose protons and electrons and easily reach higher oxidation states.[48] However, the Pourbaix diagram of $[\mathbf{Ru}^{II}-OH_2]^{2+}$ (Figure 2) is rather simple compared to that of $[Ru(tpy)(bpy)(OH_2)]^{2+}$.[48] The pH-dependent part of the Pourbaix diagram has a slope of ca. −59 mV/pH in the region of pH 2.9−12. The formation of $[\mathbf{Ru}^{III}-OH]^{2+}$ by a coupled one-proton and one-electron process is normally invoked for such a phenomenon; however, a coupled two-proton and two-electron process to form $[\mathbf{Ru}^{IV}=O]^{2+}$ is also possible, as found for *cis*-$[Ru(CNC)(n\text{-Bu-CN})(OH_2)]^{2+}$ (CNC = 2,6-bis-(*n*-butylimidazol-2′-ylidene)pyridine, *n*-Bu-CN = 2-(*n*-butylimidazol-2′-ylidene)pyridine).[76] The UV−vis spectrum of $[\mathbf{Ru}^{II}-OH_2]^{2+}$ did not change upon acid−base titration in the range of pH 1−13.5, indicating that there is no deprotonation of the coordinated water or protonation of the noncoordinating N atom of the naphthyridine part of the ligand, which is consistent with the Pourbaix diagram. The Pourbaix diagram shows that the pK_a of the one-electron-oxidized species, $[\mathbf{Ru}^{III}-OH_2]^{3+}$, is around 2.9. We will discuss in detail the disproportionation of $[\mathbf{Ru}^{III}-OH]^{2+}$ observed by pulse radiolysis in the section "Characterization of One- and Two-Electron Oxidized Intermediates". The disproportionation of the one-electron-oxidized species in the pH range above 2.9 indicates that the potential of the $[\mathbf{Ru}^{IV}=O]^{2+}/[\mathbf{Ru}^{III}-OH]^{2+}$ couple is equal to or lower than that of the $[\mathbf{Ru}^{III}-OH]^{2+}/[\mathbf{Ru}^{II}-OH_2]^{2+}$ couple, and the process corresponding to −59 mV/pH in the region of pH 2.9−12 of the Pourbaix diagram corresponds to two-electron oxidation.

The situation is different for the oxidation of $[\mathbf{Ru}^{II}-OH_2]^{2+}$ on the lower side of the pK_a of $[\mathbf{Ru}^{III}-OH_2]^{3+}$. The absence of a dependence of the potential on pH indicates that the first step is not proton coupled and thus corresponds to the formation of $[\mathbf{Ru}^{III}-OH_2]^{3+}$ (eq 3); however, we did not observe a redox couple with a slope of −118 mV/pH corresponding to the formation of $[\mathbf{Ru}^{IV}=O]^{2+}$. This differs from the case of $[Ru^{II}(tpy)(bpy)(OH_2)]^{2+}$ and $[Ru^{II}(tpy)(bpm)(OH_2)]^{2+}$ in which the first oxidation of $[Ru^{II}(tpy)(bpy)(OH_2)]^{2+}$ (or $[Ru^{II}(tpy)(bpm)(OH_2)]^{2+}$) to form $[Ru^{III}(tpy)(bpy)(OH_2)]^{3+}$ (or $[Ru^{III}(tpy)(bpm)(OH_2)]^{3+}$) is followed by a pH-dependent redox couple with the slope of −118 mV/pH corresponding to the formation of $[Ru^{IV}(tpy)(bpy)(O)]^{2+}$ (or $[Ru^{IV}(tpy)(bpm)(O)]^{2+}$). The nonobservation of the corresponding process in the case of *cis*-$[Ru(CNC)(n\text{-Bu-CN})(OH_2)]^{2+}$ was attributed previously[76] to slow electrode kinetics.

A second oxidation process (eq 5) at 1420 mV in the Pourbaix diagram was found to be pH-independent over a wide range of proton concentrations (pH 0.9−10). It should be noted that this $[\mathbf{Ru}^{V}=O]^{3+}/[\mathbf{Ru}^{IV}=O]^{2+}$ potential is much lower than those of the $[Ru^{II}(NNN)(NN)(OH_2)]^{2+}$ species (e.g., $[Ru^{II}(tpy)(bpy)(OH_2)]^{2+}$ 1800 mV,[35,36] $[Ru^{II}(tpy)(bpm)(OH_2)]^{2+}$ 1650 mV).[34] It seems that the formation of $[\mathbf{Ru}^{IV}=O]^{2+}$ at low pH is followed by the production of $[\mathbf{Ru}^{V}=O]^{3+}$ at relatively low applied potential. This may lead to a high catalytic activity for water oxidation at low overpotential.

Finally, in the pH region below ca. 0.9, the signal around 1420 mV starts overlapping with the catalytic current, making it difficult to determine the peak position, but it appears to have a −59 mV/pH slope, which corresponds to two-electron oxidation of $[\mathbf{Ru}^{III}-OH_2]^{3+}$ coupled to the loss of two protons leading to the formation of $[\mathbf{Ru}^{V}=O]^{3+}$ (eq 4b).

Theoretical Investigation of Possible Intermediates. To identify possible intermediates, we calculated geometries, energetics, and spectroscopic properties of $[\mathbf{Ru}^{II}-OH_2]^{2+}$, $[\mathbf{Ru}^{III}-OH]^{2+}$, $^1[\mathbf{Ru}^{IV}=O]^{2+}$, $^3[\mathbf{Ru}^{IV}=O]^{2+}$, $[\mathbf{Ru}^{V}=O]^{3+}$, $[\mathbf{Ru}^{III}-OOH]^{2+}$, $^3[\mathbf{Ru}^{IV}-\eta^1\text{-OO}]^{2+}$, $^1[\mathbf{Ru}^{IV}-\eta^2\text{-OO}]^{2+}$, $^1[\mathbf{Ru}^{IV}-\text{cyc-OON}]^{2+}$

Table 1. Calculated Standard Free Energies of the Species Derived from $[Ru^{II}-OH_2]^{2+}$ Involved in the Catalytic Water Oxidation Using the Large Basis[a]

system	reservoir	rel. total G^* (eV vs NHE)	ΔG^* (eV)[b]
$^1[Ru^{II}-OH_2]^{2+}$	$2H_2O$	0.000	
$^2[Ru^{III}-OH_2]^{3+}$	$2H_2O$, e^-	0.961	0.961
$^2[Ru^{III}-OH]^{2+}$	$2H_2O$, H^+, e^-	1.231	1.231
$^3[Ru^{IV}=O]^{2+}$	$2H_2O$, $2H^+$, $2e^-$	2.532	1.571
$^1[Ru^{IV}=O]^{2+}$	$2H_2O$, $2H^+$, $2e^-$	3.121	2.159
$^2[Ru^{V}=O]^{3+}$	$2H_2O$, $2H^+$, $3e^-$	4.196	1.664
$^2[Ru^{III}-OOH]^{2+}$	H_2O, $3H^+$, $3e^-$	4.397	1.865
$^3[Ru^{IV}-\eta^1\text{-}OO]^{2+}$	H_2O, $4H^+$, $4e^-$	5.551	1.355
$^1[Ru^{IV}-\eta^2\text{-}OO]^{2+}$	H_2O, $4H^+$, $4e^-$	6.125	1.929
$^1[Ru^{IV}-\text{cyc-}OON]^{2+}$ [c]	H_2O, $4H^+$, $4e^-$	6.500	2.304
$^1[Ru^{II}-OH_2]^{2+}$	O_2, $4H^+$, $4e^-$	4.760	−0.792
$^2[Ru^{III}-OH]^{2+}$	O_2, $5H^+$, $5e^-$	5.991	0.440
$^1[Ru^{II}-HOOH]^{2+}$ [c]		0.000	
$^1[Ru^{II}-OOH_2]^{2+}$ [c,d]		0.412	
$^1[Ru^{II}(NPMH^+)(pic)_2-OH_2]^{3+}$ [c]		0.000	
$^1[Ru^{II}-OH_2]^{2+}$	H^+	−0.024	

Net system reaction: $^1[Ru^{II}-OH_2]^{2+} \rightarrow {}^1[Ru^{II}-OH_2]^{2+}$, $\Delta G^* = 0$ or $^2[Ru^{III}-OH]^{2+} \rightarrow {}^2[Ru^{III}-OH]^{2+}$, $\Delta G^* = 0$

Net reservoir reaction: $2H_2O \rightarrow O_2 + 4H^+ + 4e^-$

$\Delta G^* = -4FE^o(O_2 + 4H^+ + 4e^- \rightarrow 2H_2O)$ [should be 4.92 eV, calcd 4.76 eV]

[a] The preceding superscript denotes spin multiplicity. [b] The free-energy difference between a listed species and the lowest-energy one-electron-reduced species. [c] These species are not likely involved in the water-oxidation reaction but are listed here for energy comparison purposes. [d] According to our DFT calculations, one of the protons of this species is transferred to form $[Ru^{II}(NPMH^+)(pic)_2-OOH]^{2+}$ (see Supporting Information).

(i.e., a $[Ru^{IV}-\eta^1\text{-}OO]^{2+}$ species with a strong interaction with the noncoordinating N atom of the naphthyridine ligand), $[Ru^{II}-HOOH]^{2+}$, and $[Ru^{II}-OOH_2]^{2+}$ (interestingly, one of the protons of this species is transferred to form $[Ru^{II}(NPMH^+)(pic)_2-OOH]^{2+}$). The calculated standard free energies are listed in Table 1. The superscript number at the beginning of each species designation represents the spin multiplicity of that species. The important geometric and spectroscopic parameters are summarized in Table S1 (Supporting Information). We will discuss these results when we describe the experimental data. All UV−vis "stick spectra" from TD-DFT calculations were convoluted with a Gaussian broadening function with a width of 0.18 eV.

Characterization of One- and Two-Electron Oxidized Intermediates. Ce(IV) is frequently used as a sacrificial oxidant for catalyzed water oxidation. The reaction between $[Ru^{II}-OH_2]^{2+}$ and Ce(IV) was examined at pH 1 in the presence of triflic acid. As seen in Figure 3a, titration of dilute acidic solutions of $[Ru^{II}-OH_2]^{2+}$ (8×10^{-7} M, 0.1 M triflic acid) with Ce(IV) shows gradual removal of the starting material and formation of the oxidized species upon consumption of ca. 2.7 equiv of Ce(IV). The presence of several clear isosbestic points indicates that the final product is produced without significant accumulation of the intermediate one-electron oxidized species. Additional Ce(IV) does not lead to any change in the spectrum. The formation of the oxidized species is reversible in dilute acidic solutions ($<10^{-6}$ M), and $[Ru^{II}-OH_2]^{2+}$ can be almost completely recovered upon the addition of ferrous ammonium sulfate as a reducing reagent. The small amount of the starting complex corresponding to the incomplete recovery of the (green) spectrum vs the (blue) spectrum in Figure 3b after back-titration with ferrous ammonium sulfate might be due to a small amount of precipitation of $[Ru^{II}-OH_2]^{2+}$ over time or the chemical reactivity of the oxidized species.

Analysis of the Pourbaix diagram (Figure 2) shows that at pH 1 $[Ru^{IV}=O]^{2+}$ may exist in equilibrium with $[Ru^{V}=O]^{3+}$. We estimate the ratio of $[Ru^{V}=O]^{3+}/[Ru^{IV}=O]^{2+}$ at pH 1 to be about 1:1 owing to only a few millivolts separation between the two species. This may be the reason we needed to add more than 2 equiv of Ce(IV) to obtain the final spectrum (blue) in Figure 3a.

The rate of the reaction between $[Ru^{II}-OH_2]^{2+}$ and an excess of Ce(IV) was monitored by following the spectral change in the 2−100 ms time window using a stopped-flow apparatus. The disappearance of the absorption features characteristic of $[Ru^{II}-OH_2]^{2+}$ was observed, but no intermediate one-electron-oxidized species was observed (Figure S2, Supporting Information). From the rate of disappearance of the MLCT band of $[Ru^{II}-OH_2]^{2+}$ at ca. 610 nm, a rate constant of $(2.0 \pm 0.3) \times 10^4\ M^{-1}\ s^{-1}$ was obtained. It is not unusual for Ru(II) polypyridyl complexes to react rather slowly with Ce^{IV}, and rate constants as low as $2 \times 10^2\ M^{-1}\ s^{-1}$ (at pH 1) have been reported.[34] The one-electron-oxidized species $[Ru^{III}-OH_2]^{3+}$ was not observed spectroscopically in our experiments at pH 1, similar to findings reported previously.[34]

Observation of One- and Two-Electron Oxidized Intermediates by Pulse Radiolysis. Ce(IV) oxidation at pH 1 may be complicated owing to the recent finding of its noninnocent nature as a one-electron oxidant.[36,77] We therefore studied the formation and reactivity of the one- and two-electron-oxidized species to elucidate these properties in the high pH range using the pulse radiolysis technique. Pulse radiolysis allows the production of various redox active species in solution and provides a means for following chemical reactivity using time-resolved UV−vis spectroscopy. The carbonate radical was chosen as the sacrificial one-electron oxidant. The redox potential of the carbonate radical (1.59 V vs NHE)[78] is similar to the potential of Ce(IV) with HNO_3 (1.61 V vs NHE at

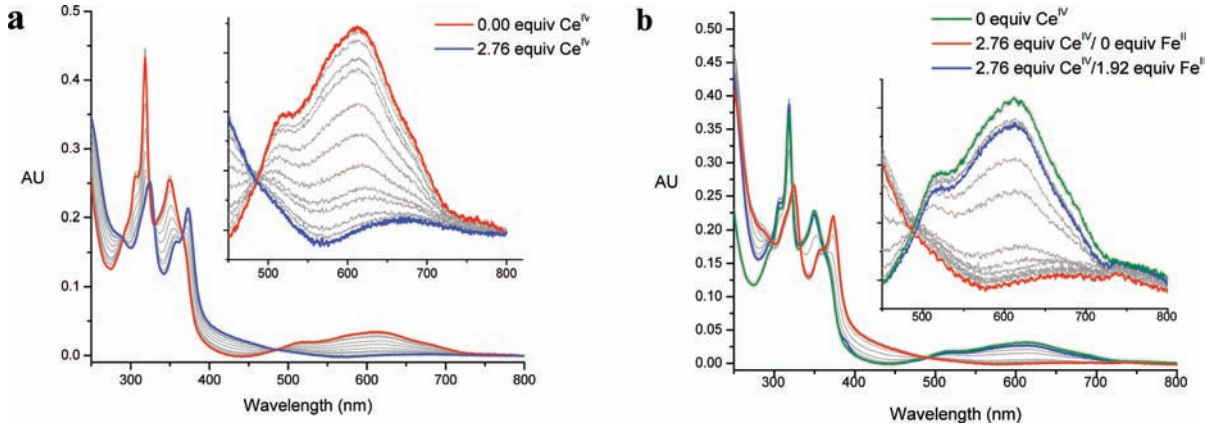

Figure 3. (a) Titration of $[\mathbf{Ru}^{II}-OH_2]^{2+}$ (8×10^{-7} M, 10 cm path cell) with Ce(IV) and (b) back-titration of 2-electron-oxidized species with ferrous ammonium sulfate in water at pH 1.

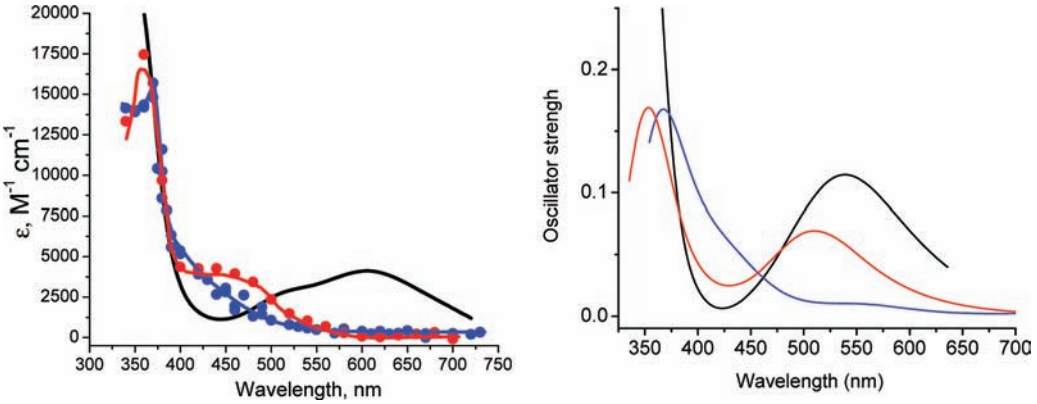

Figure 4. Experimental (left) and calculated (right) UV−vis spectra of $[Ru^{II}-OH_2]^{2+}$ (black), one-electron oxidized species (red), and two-electron oxidized species (blue). The calculated spectrum for the two-electron oxidized species is that of $^3[Ru^{IV}=O]^{2+}$.

pH 0).[72] The carbonate radical can be produced efficiently only at pH above 9 since the pK_a of the bicarbonate ion is around 10. Creating oxidative conditions during radiolysis in acidic solutions, below ca. pH 3, where the yield of the hydrogen atom becomes significant, proves problematic. Because the hydrogen atom exhibits diverse reactivity, its production in this particular study was avoided.

The reaction between the carbonate radical and $[\mathbf{Ru}^{II}-OH_2]^{2+}$ at pH 10 yielded the one-electron-oxidized species (eq 6) with a distinct absorption spectrum (Figure 4, left) which agrees with the spectrum of $[\mathbf{Ru}^{III}-OH]^{2+}$ obtained using TD-DFT-(B3LYP) calculations (Figure 4, right). The one-electron-oxidized species is produced with a rate constant of $(2.8 \pm 0.5) \times 10^9$ M^{-1} s^{-1} (with ionic strength 0.06 M).

$$CO_3^{\bullet-} + [\mathbf{Ru}^{II}-OH_2]^{2+} \rightarrow HCO_3^- + [\mathbf{Ru}^{III}-OH]^{2+} \quad (6)$$

$$2[\mathbf{Ru}^{III}-OH]^{2+} \rightarrow [\mathbf{Ru}^{II}-OH_2]^{2+} + [\mathbf{Ru}^{IV}=O]^{2+} \quad (6a)$$

$$CO_3^{\bullet-} + [\mathbf{Ru}^{III}-OH]^{2+} \rightarrow HCO_3^- + [\mathbf{Ru}^{IV}=O]^{2+} \quad (7)$$

$$2H_2O + 2CO_3^{\bullet-} \rightarrow 2CO_3^{2-} + H_2O_2 + 2H^+ \quad (8)$$

The one-electron-oxidized species, $[\mathbf{Ru}^{III}-OH]^{2+}$, produced in the pulse radiolysis experiment is not stable and slowly disappears on the time scale of ca. 1 min ($k_{disp} = (6.5 \pm 0.5) \times 10^3$ M^{-1} s^{-1}). The disappearance of the absorption at 450 nm (attributed to $[\mathbf{Ru}^{III}-OH]^{2+}$) is concomitant with partial recovery of the 610 nm band and is described by a second-order rate law (Figure S3−S4, Supporting Information). This reaction was assigned to disproportionation of the one-electron-oxidized species to produce 1 equiv of the starting material and 1 equiv of the two-electron-oxidized species (eq 6a). These observations suggest that the $Ru^{III/II}$ couple is equal to or more positive than the $Ru^{IV/III}$ couple. As will be discussed later, theoretical results on these potentials are consistent with this interpretation (see the "Theoretical Analysis of the Electrochemical Oxidation of $[\mathbf{Ru}^{II}-OH_2]^{2+}$" section below).

The reaction of $[\mathbf{Ru}^{II}-OH_2]^{2+}$ with an excess of the carbonate radical was also studied in an attempt to produce a two-electron-oxidized species (eqs 6 and 7). This reaction can be described in terms of two stepwise one-electron oxidations. In addition, the carbonate radical is known to react with water according to eq 8, which is second order in the carbonate radical. The data measured for reactions between $[\mathbf{Ru}^{II}-OH_2]^{2+}$ and an excess of the carbonate radical were fitted by a kinetic model based on eqs 6− 8 using numerical integration.[79] The rate constant corresponding to the first oxidation was fixed at the value, $k_6 = (2.8 \pm 0.5) \times 10^9$ M^{-1} s^{-1}, that was obtained independently from experiments under pseudo-first-order conditions (with an excess of $[\mathbf{Ru}^{II}-OH_2]^{2+}$). The traces obtained from these fits agree well with experimental data. For example, the behavior of

the 450 nm trace is typical of an intermediate species B in an A-to-B-to-C kinetic model and is well described by the proposed mechanism (Figure S5, Supporting Information). Further kinetic analysis based on the proposed model indicates that nearly complete conversion of $[\mathbf{Ru}^{II}-OH_2]^{2+}$ into the two-electron-oxidized species should be achieved using a minimum of 2.5 equiv of the carbonate radical relative to $[\mathbf{Ru}^{II}-OH_2]^{2+}$. The rate constants obtained from the fits with the kinetic model at λ = 450 nm are: $k_6 = (2.8 \pm 0.5) \times 10^9\ M^{-1}\ s^{-1}$; $k_7 = (2.6 \pm 0.3) \times 10^7\ M^{-1}\ s^{-1}$; $k_8 = (7.9 \pm 0.9) \times 10^6\ M^{-1}\ s^{-1}$. The deviation in rate constants was within 15% for all wavelengths. Our value of the $CO_3^{\bullet-}$ decay (k_8) was in good agreement with reported values.[80,81]

Interestingly, the spectra of the two-electron-oxidized species produced at pH 1 by Ce(IV) and at pH 10 by the carbonate radical match fairly well (see Figure S6, Supporting Information), indicating that the same species can be formed over a wide pH range. Since the Pourbaix diagram of $[\mathbf{Ru}^{II}-OH_2]^{2+}$ (Figure 2) reveals that several species might be in equilibrium (i.e., $[\mathbf{Ru}^{III}-OH_2]^{3+}$, $[\mathbf{Ru}^{IV}=O]^{2+}$, and $[\mathbf{Ru}^{V}=O]^{3+}$) at pH 1, and the final spectrum of the two-electron-oxidized species is obtained by an addition of 2.7 equiv of Ce(IV), the spectra of $[\mathbf{Ru}^{IV}=O]^{2+}$ and $[\mathbf{Ru}^{V}=O]^{3+}$ might be very similar. We should point out again that additional Ce(IV) beyond 2.7 equiv does not change the spectrum. In fact, Berlinguette et al. have reported that the spectra of Ru (IV) and Ru(V) species of Ru(trp)(bpy)-(O) are very similar.[35,36]

Theoretical characterization of $[\mathbf{Ru}^{IV}=O]^{2+}$ is described in the Supporting Information. It should be noted that a weak band is experimentally observed around 670 nm (Figure 3), which probably corresponds to the 747 nm band predicted theoretically for the triplet state (Figure S7, Supporting Information).

Characterization of the Two-Electron-Oxidized Species in CH_3CN. While dilute ($<10^{-5}$ M) acidic solutions of the two-electron-oxidized species can be characterized by UV−vis spectroscopy and ESI-MS spectrometry immediately after their formation, more concentrated samples are not stable in aqueous media. To characterize the two-electron-oxidized species in the absence of water, a sample was prepared by rapid mixing of aqueous $[\mathbf{Ru}^{II}-OH_2]^{2+}$ with 2 equiv of Ce(IV) in triflic acid (pH 1) followed by rapid precipitation with NH_4PF_6. The resulting solid precipitate was vacuum-dried and dissolved in dry acetonitrile and characterized by ESI-MS and UV−vis spectroscopy. The UV−vis and MS spectra were consistent with $[\mathbf{Ru}^{IV}=O]^{2+}$ but not $[\mathbf{Ru}^{II}-NCCH_3]^{2+}$. We also prepared $[Ru^{II}(tpy)(bpy)(O)]^{2+}$ by bulk electrolysis in 0.1 M deuterated triflic acid in D_2O at 1370 mV vs NHE. This species is stable even at high concentration. The ^{1}H NMR spectra of $[Ru^{II}(tpy)(bpy)(O)]^{2+}$ in D_2O and $[\mathbf{Ru}^{IV}=O]^{2+}$ in CD_3CN are shown in Figures S13 and S14 (Supporting Information), respectively. Both spectra are characteristic of a paramagnetic species, with several resonances in the negative parts per million region that are typical of ruthenium oxo complexes,[82−87] consistent with our theoretical results with the assignment as $^3[\mathbf{Ru}^{IV}=O]^{2+}$ but not $^3[\mathbf{Ru}^{III}-O^{\bullet-}]^{2+}$. However, a low-spin Ru=O complex has recently been reported.[88] The cyclic voltammogram of $[\mathbf{Ru}^{IV}=O]^{2+}$ in CH_3CN shows a reversible redox couple with $E_{1/2}$ = 1380 mV (Figure S15, Supporting Information).

Products of the Electrochemical Four-Electron Oxidation of $[\mathbf{Ru}^{II}-OH_2]^{2+}$. Aqueous solutions of $[\mathbf{Ru}^{II}-OH_2]^{2+}$ were electrolyzed at 1260 mV vs NHE at pH 1 (0.1 M triflic acid) and 1150 mV at pH 6 (10 mM sodium phosphate). Both solutions contained 20% by volume of trifluoroethanol to maintain solubility of the complex at a concentration of about 1 mM. Exhaustive electrolysis at constant potential (i.e., until the final current was less than 1% of the initial current) yielded a red colored solution with a Coulomb count corresponding to the *net four-electron oxidation* of $[\mathbf{Ru}^{II}-OH_2]^{2+}$, despite applying potentials much less than that of the $[\mathbf{Ru}^{V}=O]^{3+}/[\mathbf{Ru}^{IV}=O]^{2+}$ couple (1420 mV). The results were similar for both high and low pH experiments.

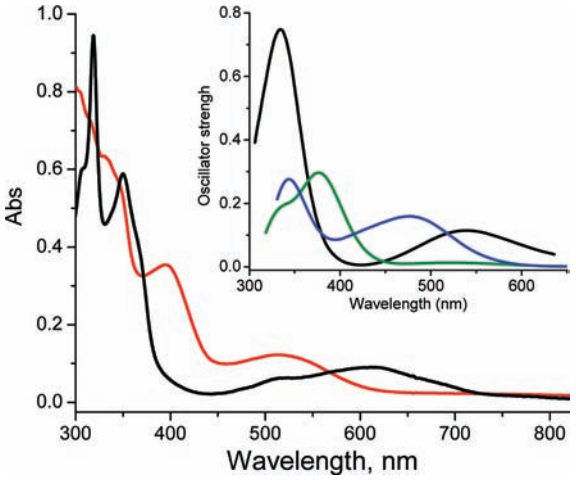

Figure 5. UV−vis absorption spectrum of $[\mathbf{Ru}^{II}-OH_2]^{2+}$ (black) and species formed after bulk electrolysis of $[\mathbf{Ru}^{II}-OH_2]^{2+}$ in water at pH 6 at 1150 mV vs NHE (red). Inset: Calculated spectra of $[\mathbf{Ru}^{II}-OH_2]^{2+}$, $^3[\mathbf{Ru}^{IV}-\eta^1\text{-}OO]^{2+}$ (blue), and $^1[\mathbf{Ru}^{IV}-\eta^2\text{-}OO]^{2+}$ (green).

The species produced during the bulk electrolysis experiment has a distinct absorption spectrum with the metal-to-ligand charge transfer (MLCT) band (with some contribution from tpy intraligand transitions) blue-shifted ca. 80 nm compared to $[\mathbf{Ru}^{II}-OH_2]^{2+}$ (Figure 5). The calculated spectrum of $^3[\mathbf{Ru}^{IV}-\eta^1\text{-}OO]^{2+}$ seems to match well; however, we cannot exclude the possibility of a mixture of $^3[\mathbf{Ru}^{IV}-\eta^1\text{-}OO]^{2+}$ and $^1[\mathbf{Ru}^{IV}-\eta^2\text{-}OO]^{2+}$. The ESI-MS analysis of the solution obtained after electrolysis indicates the presence of a species with m/z = 355 and 710, which correspond to $[\mathbf{Ru}^{IV}-(^{16}O^{16}O)]^{2+}$ (M−1 = 710). The isotope pattern of this proposed structure matches well the observed pattern (Figure S16, Supporting Information). Finally, electrolysis of $[\mathbf{Ru}^{II}-OH_2]^{2+}$ in $H_2{}^{18}O$ (>95% ^{18}O) yields a species with m/z = 357 and 714 corresponding to the structure $[\mathbf{Ru}^{IV}-(^{18}O^{18}O)]^{2+}$ (M−1 = 714; Figure S17, Supporting Information), confirming that the source of O atoms is water. It should be noted that similar bulk electrolysis experiments were conducted with dilute solutions (ca. 75 μM) of $[\mathbf{Ru}^{II}-OH_2]^{2+}$ but in the absence of trifluoroethanol. Although an accurate Coulomb count was not possible due to the low concentration of $[\mathbf{Ru}^{II}-OH_2]^{2+}$, the UV−vis and mass spectra of the electrolysis product were identical to those obtained in experiments with trifluoroethanol as a cosolvent.

The resonance Raman spectra of $[\mathbf{Ru}^{II}-OH_2]^{2+}$ and the product obtained by bulk electrolysis of $[\mathbf{Ru}^{II}-OH_2]^{2+}$, presumably $[\mathbf{Ru}^{IV}-OO]^{2+}$, are shown in Figure S18 (Supporting Information). The peak positions in these two spectra are similar, except for two new bands at 547 and 930 cm^{-1} (and changes in intensities of a few extra bands in the 1250−1600 cm^{-1} region) observed in the spectrum of the oxidized species. The difference in relative intensities of the Raman bands of the starting material and the oxidized species is most likely due to differing resonance enhancement of the vibrational transitions in these two species. The resonance Raman spectra of $[\mathbf{Ru}^{IV}-{}^{16}O^{16}O]^{2+}$ and

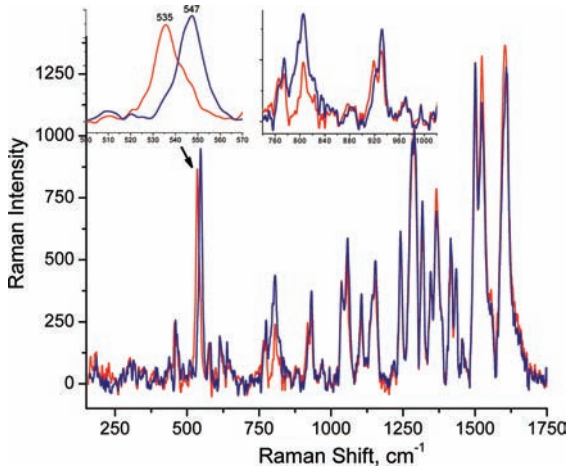

Figure 6. Resonance Raman spectra of $[Ru^{II}-OH_2]^{2+}$ after bulk electrolysis at 1150 mV in $H_2{}^{16}O$ (blue trace) and $H_2{}^{18}O$ (red trace).

$[Ru^{IV}-{}^{18}O^{18}O]^{2+}$ shown in Figure 6 are almost identical except for the red shift of the low-energy vibration (547 → 535 cm^{-1}) and the shifts of several bands in the 760−960 cm^{-1} region (the top right spectra in Figure 6). Due to the overlapping vibrational modes of the ligands, it is not easy to observe the O−O and Ru=O stretching frequencies. The Raman bands at 930 and 800 cm^{-1} seem to shift to 920 and 760 cm^{-1}, respectively, by changing the sample preparation in $H_2{}^{16}O$ to $H_2{}^{18}O$. The NMR spectrum of $[Ru^{IV}-OO]^{2+}$ in D_2O is indicative of the presence of a paramagnetic center together with sharp signals, which may suggest an existence of $^1[Ru^{IV}-\eta^2\text{-}OO]^{2+}$ in a mixture with the triplet species (Figure S19, Supporting Information).

Reactivity of the Two-Electron-Oxidized Species at pH 1. As presented earlier, *very* dilute acidic solutions of the two-electron-oxidized species (8×10^{-7} M) prepared by rapid mixing of $[Ru^{II}-OH_2]^{2+}$ with 2 equiv of Ce(IV) appear to be stable on the time scale of several minutes in the absence of Ce(IV). While such samples may possibly be an equilibrium mixture of $[Ru^{IV}=O]^{2+}$ and other species, *here we simply denote them as* $[Ru^{IV}=O]^{2+}$. In higher concentrations (above ca. 10^{-5} M), the formation of approximately equal concentrations of $[Ru^{IV}-OO]^{2+}$ and $[Ru^{II}-OH_2]^{2+}$ was observed (Figure 7) in 2 h. These products were identified by UV−vis spectroscopy and ESI-MS analysis. The absorption spectra of $[Ru^{IV}-OO]^{2+}$ and $[Ru^{III}-OOH]^{2+}$ were predicted by TD-DFT(B3LYP) calculations, and that of $^3[Ru^{IV}-\eta^1\text{-}OO]^{2+}$ matches better in terms of the spectral shape and oscillator strength (Figure S20, Supporting Information). We should note, however, that $[Ru^{III}-OOH]^{2+}$ cannot be totally excluded as the assignment of the oxidized species since the difference in m/z is only 0.5 units and the calculated spectrum of $^1[Ru^{IV}-\eta^2\text{-}OO]^{2+}$ may not be accurate due to the open-shell singlet character missing from its calculated electronic structure. The kinetics of the formation of these products appear to be complex but certainly depend on the initial concentration of $[Ru^{II}-OH_2]^{2+}$ (Figure S21, Supporting Information). ESI-MS of the reaction mixture injected immediately after preparation by an addition of 2 equiv of Ce(IV) to $[Ru^{II}-OH_2]^{2+}$ at pH 1 shows m/z 356.8 for $[Ru^{IV}=O\cdots OH_2]^{2+}$ together with m/z 348.3 probably for $[Ru^{II}-OH_2]^{2+}$ and m/z 355.1 for $[Ru^{IV}-OO]^{2+}$ (Figure S22, Supporting Information, top panel). The intensity of signals in the range of m/z 354−359 cannot be explained by the isotope pattern of a single species and changes in complicated ways with time. The m/z signal corresponding to $[Ru^{V}=O]^{3+}$ was not

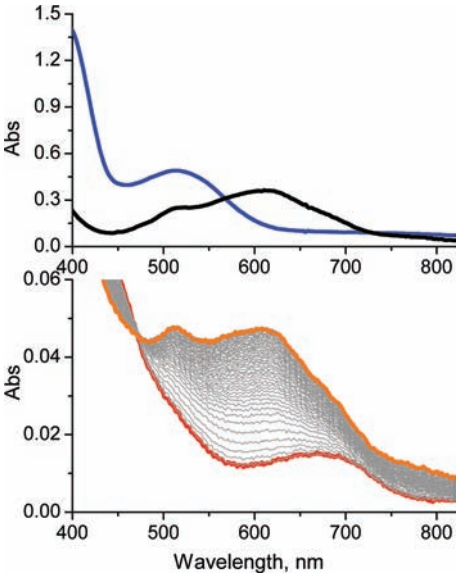

Figure 7. Bottom: spectral evolution of $[Ru^{IV}=O]^{2+}$ (25 μM) at pH 1 (triflic acid) that indicates formation of an equal amount of $[Ru^{II}-OH_2]^{2+}$ and $[Ru^{IV}-OO]^{2+}$. Red curve is the spectrum of $[Ru^{IV}=O]^{2+}$, and the orange curve is the final spectrum. The spectral interval is 2 min (the experimental time scale is ca. 120 min). Top: spectra of $[Ru^{II}-OH_2]^{2+}$ (black) and $[Ru^{IV}-OO]^{2+}$ obtained by bulk electrolysis of $[Ru^{II}-OH_2]^{2+}$ (blue).

observed most likely due to its low initial concentration and its fast reaction with a water molecule. The m/z 347.8 was observed when $[Ru^{IV}=O]^{2+}$ was precipitated with NH_4PF_6 immediately after preparation by addition of 2 equiv of Ce(IV) to $[Ru^{II}-OH_2]^{2+}$ in acidic aqueous solution (pH 1, triflic acid), dried under vacuum, and transferred into dry acetonitrile (Figure S23, Supporting Information, bottom panel).

The final species observed in experiments with 2, 3, and 4 (Figures S23−S25, Supporting Information) equiv of Ce(IV) have m/z 356.4. We cannot identify whether these are products of ionization reactions, but $[Ru^{III}-OOH]^{2+}$ (356.4) and $[Ru^{II}-HOOH]^{2+}$ (356.9) are possible products.

Electrochemical Products Generated via $[Ru^{IV}=O]^{2+}$. The bulk electrolysis of $[Ru^{II}-OH_2]^{2+}$ discussed in the "Products of the Electrochemical Four-Electron Oxidation of $[Ru^{II}-OH_2]^{2+}$" section indicates that our expected product $[Ru^{IV}=O]^{2+}$ changed to $[Ru^{IV}-OO]^{2+}$ by an additional net two-electron oxidation at 154 mV above $E_{1/2}(Ru^{IV}=O/Ru^{II}-OH_2)$ and 270 mV below $E_{1/2}(Ru^{V}=O/Ru^{IV}=O)$ at pH 6. The square wave voltammetry of the bulk electrolysis product with net four-electron oxidation at 1150 mV shows the most intense peak around 700 mV, which is likely the redox reaction shown as eq 9, together with weak peaks around 1030 and 1170 mV (Figure 8). We carried out further cyclic and square wave voltammograms of $[Ru^{II}-OH_2]^{2+}$ at pH 6 to understand this phenomenon and to detect the product(s). The comparison of the anodic and cathodic voltammetric scans during electrochemical studies of $[Ru^{II}-OH_2]^{2+}$ revealed the formation of a new species when the potential is scanned from ca. 1500 to 250 mV at pH 6 (Figure 8).

The Pourbaix diagram in Figure 9 obtained from the cathodic scans from 1240 mV at various pH shows new pH-dependent features (e.g., the green line), indicating that the electrochemical product is a conjugate acid. Increasing the quiet time at the beginning of each cathodic scan at 1240 mV led to an increase in

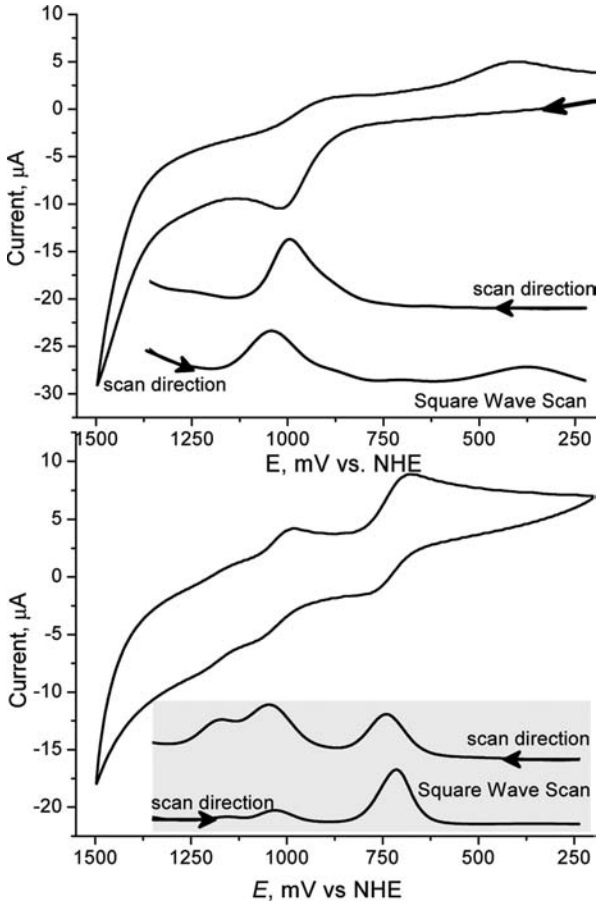

Figure 8. Top panel: Cyclic and square wave voltammograms of $[\mathbf{Ru}^{II}-OH_2]^{2+}$ in water (pH 6). Bottom panel: Cyclic and square wave voltammograms of the bulk electrolysis product (pH 6) at 1150 mV vs NHE. The inset shows square wave anodic (top) and cathodic (bottom) scans.

the electrochemical products. The current at the pH-dependent potential shown by the red line in Figure 9 appears almost negligible in the first few scans, but the intensity gradually increases with repeated cathodic scans. This suggests that the initial species, which is likely $[\mathbf{Ru}^{III}-OOH]^{2+}$, is produced at an applied potential above $E_{1/2}(\mathbf{Ru}^{IV}=O/\mathbf{Ru}^{II}-OH_2)$ and is reduced to $[\mathbf{Ru}^{II}-OOH]^{+}$ (and/or its protonated species at low pH) at potentials shown by the green line (eqs 10 and 11).

It should be noted that the applied potential of 1240 mV, i.e., 180 mV less positive than that for $E_{1/2}(Ru^{V}/Ru^{IV})$, seems sufficient to carry out the reaction shown as the net process in eq 9 during the quiet time before the cathodic scans, and eventually the reactions shown as eqs 10 and 11 seem to take place.

$$[\mathbf{Ru}^{IV}=O]^{2+} + H_2O - e^- \rightarrow [\mathbf{Ru}^{III} - OOH]^{2+} + H^+ \quad (9)$$

$$[\mathbf{Ru}^{III} - OOH]^{2+} + e^- \rightarrow [\mathbf{Ru}^{II} - OOH]^{+} \quad (10)$$

$$[\mathbf{Ru}^{III} - OOH]^{2+} + e^- + H^+ \rightarrow [\mathbf{Ru}^{II} - HOOH]^{2+} \quad (11)$$

Interestingly, the bulk electrolysis product exhibits currents at the potential corresponding to the red line without any current at the lower potential of the green line. This discrepancy seems to suggest that the species prepared by bulk electrolysis is possibly $^1[\mathbf{Ru}^{IV}-\eta^2\text{-}OO]^{2+}$. The geometric conversion from the η^2 mode

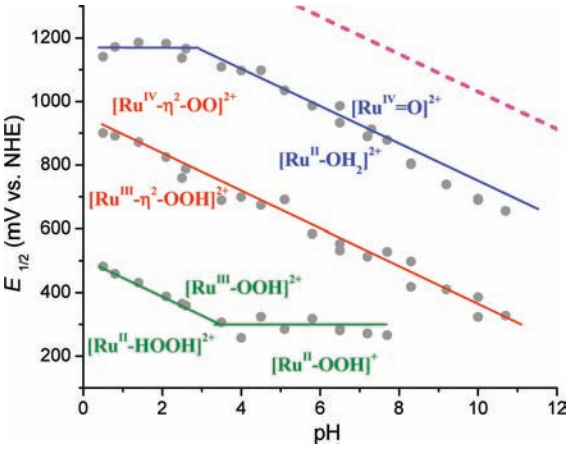

Figure 9. Pourbaix diagram of the species produced by electrochemical oxidation of $[\mathbf{Ru}^{II}-OH_2]^{2+}$ in water after holding the potential at 1240 mV for 2 s and scanning in the cathodic direction. The magenta dotted line corresponds to the calculated potential for $[\mathbf{Ru}^{IV}=O]^{2+} + H_2O - e^- \rightarrow [\mathbf{Ru}^{III}-OOH]^{2+} + H^+$ and was not observed.

to the η^1 mode for the formation of $[\mathbf{Ru}^{III}-OOH]^{2+}$ may not take place on the time scale of the square-wave voltammogram. The broad signals observed in the NMR might be due to a small amount of coexisting geometric isomer, $^3[\mathbf{Ru}^{IV}-\eta^1\text{-}OO]^{2+}$, and/or contamination by $^2[\mathbf{Ru}^{III}-OOH]^{2+}$, together with the sharp signals of $^1[\mathbf{Ru}^{IV}-\eta^2\text{-}OO]^{2+}$. We will discuss the nature of this species in the Discussion section.

No oxygen production from $[\mathbf{Ru}^{IV}-OO]^{2+}$ was found under our experimental conditions in the absence of an added oxidant. The decomposition of $[\mathbf{Ru}^{IV}-OO]^{2+}$ in water (pH 6) can be observed after several hours by following the changes in the UV−vis absorption spectrum, and complete conversion was achieved after ca. two weeks (Figure S26, Supporting Information). The UV−vis spectrum of the decomposition product does not correspond to $[\mathbf{Ru}^{II}-OH_2]^{2+}$ but closely resembles it. The ESI-MS analysis of the product indicates the presence of a species corresponding to the formula $[\mathbf{Ru}^{II}-OOH]^{+}$ (Figure S27, Supporting Information). The ^{1}H NMR spectrum (in D_2O) confirms the assignment to diamagnetic $[\mathbf{Ru}^{II}-OOH]^{+}$ based on the number of protons contained in organic ligands and sharp signals (Figure S28, Supporting Information, bottom) and is different from that of $[\mathbf{Ru}^{II}-OH_2]^{2+}$ reported previously (Figure S28, Supporting Information, top).[28] The NMR of the product(s) indicates $[\mathbf{Ru}^{II}-OOH]^{+}$ as an almost pure product and supports the reaction shown in eq 10.

Theoretical Analysis of the Electrochemical Oxidation of $[\mathbf{Ru}^{II}-OH_2]^{2+}$. Calculations of the absolute standard free energy of species postulated to be involved in the catalytic water oxidation cycle were carried out to construct the free-energy profile of the catalytic reaction and relevant features of Pourbaix diagrams for comparison with the experimental results. The results for the species we have identified as catalytic intermediates are summarized in Table 1. The "system" species in the second and last rows of the table are identical, i.e., $[\mathbf{Ru}^{III}-OH]^{2+}$. The proposed catalytic step from $[\mathbf{Ru}^{IV}=O]^{2+}$ to $[\mathbf{Ru}^{III}-OOH]^{2+}$ may occur directly or with $[\mathbf{Ru}^{V}=O]^{3+}$ as an intermediate, as discussed below. Also, a molecule of water solvent could possibly displace triplet O_2 from either singlet or triplet $[\mathbf{Ru}^{IV}-OO]^{2+}$ species (the singlet would require spin−orbit coupling and would likely be an activated process) in an exothermic reaction to regenerate singlet $[\mathbf{Ru}^{II}-OH_2]^{2+}$. Finally, O_2 evolution could result from

the oxidation of singlet or triplet $[\mathbf{Ru}^{IV}-OO]^{2+}$ to produce $^2[\mathbf{Ru}^{III}-OH]^{2+}$ as evidenced in an attempted geometry optimization of "$^2[\mathbf{Ru}^{V}-\eta^1\text{-}OO]^{3+}$", the $1e^-$ oxidized species of $^3[\mathbf{Ru}^{IV}-\eta^1\text{-}OO]^{2+}$, in which the $^3O_2$ moiety is spontaneously expelled from the metal center (Ru−O distances increasing from 2.03 and 2.12 Å to 4.47 and 4.62 Å) and while the explicit molecule of H_2O solvent hovers closer to the metal center (Ru−O distance decreasing from 4.85 to 4.54 Å).

The species listed in the "reservoir" column of the table are those that must eventually be transferred to a system species from the solution (i.e., the two water molecules that will eventually be oxidized to O_2) and those that are removed from the system to the solution or to the gas phase (i.e., protons, electrons, and eventually O_2) along the catalytic pathway. Consideration of the sum of the free energies of the system and reservoir species for each intermediate allows the construction of a meaningful standard free energy profile along the reaction pathway, as shown in the "rel. total G^* (eV vs NHE)" column of Table 1. It is clear that the net reaction around the catalytic cycle in the system is

$$^2[\mathbf{Ru}^{III}-(OH)\cdot H_2O]^{2+} \rightarrow {}^2[\mathbf{Ru}^{III}-(OH)\cdot H_2O]^{2+},\ \Delta G^* = 0$$

while the net reaction in the reservoir is

$$2H_2O \rightarrow O_2 + 4H^+ + 4e^-,\ \Delta G^\circ = 4FE^\circ(\mathrm{ORR})$$

where ORR stands for the oxygen reduction reaction.

The column with the heading "rel. total G^* (eV vs NHE)" in Table 1 references the electron transfer steps to the normal hydrogen electrode (NHE), which is evaluated here (using the methodogy described in the Supporting Information) to be 4.157 eV in aqueous solution. The calculated value of the standard free energy change for the ORR, again using the same methodology, is 4.760 eV and is completely independent of the catalyst calculations. It results only from the calculated values of the free energies of $O_2(g)$ and H_2O (liquid), the values of the standard free energies of the solvated proton and gas-phase electron used, and the value of the absolute potential of the normal hydrogen electrode (NHE). The error (−0.156 eV, or −0.039 eV per electron) in the calculated standard free energy change of the ORR (4.916 eV) is most likely due to DFT doing a poor job on the electronic energy of the ground state of $O_2(g)$. This estimated error in the last step of the cycle may account for the underestimated value of the standard free energy change, which contrasts with the experimental observations.

The last column of Table 1, under the heading "ΔG^* (eV)", lists the standard free-energy changes for the various steps in the proposed catalytic mechanism. The standard free-energy difference listed for a given species is relative to the corresponding one-electron-reduced species with the lowest free energy. We do not imply that the "assignment" of the species with lowest calculated free energy is necessarily correct (see discussion regarding $[\mathbf{Ru}^{IV}=O]^{2+}$ above) but that there is a species of that chemical formula that has at least as low an energy as that listed. All the electron-transfer steps are proton coupled (PCET) except for $[\mathbf{Ru}^{IV}=O\cdot H_2O]^{2+} \rightarrow [\mathbf{Ru}^{V}=O\cdot H_2O]^{3+}$, which is a simple electron transfer step which requires a subsequent proton transfer step to reach $[\mathbf{Ru}^{III}-(OOH)\cdot H_2O]^{2+}$. Therefore, all the free-energy changes except for the $[\mathbf{Ru}^{IV}=O\cdot H_2O]^{2+} \rightarrow [\mathbf{Ru}^{V}=O\cdot H_2O]^{3+}$ and $[\mathbf{Ru}^{II}-OH_2]^{2+} \rightarrow [\mathbf{Ru}^{III}-OH_2]^{3+}$ steps will be pH dependent, with $\Delta G_{ox} = \Delta G_{ox}^* - 0.059\cdot pH$ relative to NHE. The computed results suggest that the step $[\mathbf{Ru}^{IV}=O\cdot H_2O]^{2+} \rightarrow [\mathbf{Ru}^{V}=O\cdot H_2O]^{3+}$ would occur at a lower applied potential than for the $[\mathbf{Ru}^{IV}=O\cdot H_2O]^{2+} + H_2O \rightarrow [\mathbf{Ru}^{III}-(OOH)\cdot H_2O]^{2+} + H^+$ step at low pH but that the subsequent addition of H_2O and removal of a proton would be slightly endothermic. At pH above ca. 3.5, the calculations predict that the potential for the direct $[\mathbf{Ru}^{IV}=O\cdot H_2O]^{2+} + H_2O \rightarrow [\mathbf{Ru}^{III}-(OOH)\cdot H_2O]^{2+} + H^+$ step would drop below that for $[\mathbf{Ru}^{IV}=O\cdot H_2O]^{2+} \rightarrow [\mathbf{Ru}^{V}=O\cdot H_2O]^{3+}$ (Figure 10).

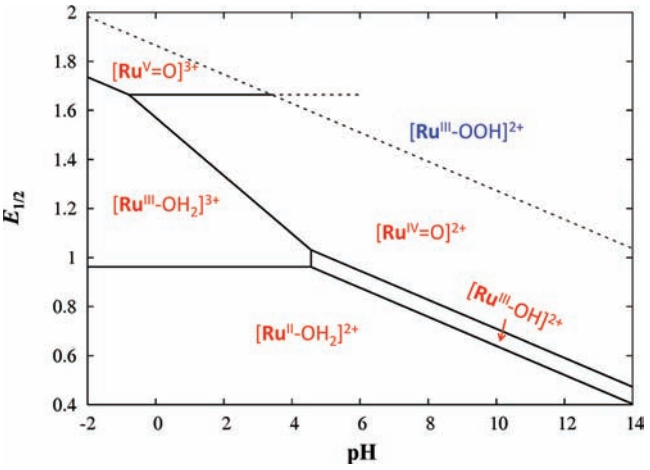

Figure 10. Calculated Pourbaix diagram for electrochemical oxidation of $[\mathbf{Ru}^{II}-OH_2]^{2+}$ in water.

The Pourbaix diagram constructed from the energies of DFT optimized structures of various redox and acid−base states of species $[\mathbf{Ru}^{II}-OH_2\cdot H_2O]^{2+}$ is shown in Figure 10. A similar, though somewhat simpler, diagram based only on the results of our calculations with the small basis set, which exhibits the same two-electron, two-proton nature of the oxidation of $[\mathbf{Ru}^{II}-OH_2\cdot H_2O]^{2+}$ to $[\mathbf{Ru}^{IV}=O\cdot H_2O]^{2+}$ as in our experiments, is presented in Figure S29 (Supporting Information). The Pourbaix diagram in Figure 10 indicates sequential $1e^-/1H^+$ oxidation steps from $[\mathbf{Ru}^{II}-OH_2]^{2+}$ to $[\mathbf{Ru}^{IV}=O]^{2+}$ separated by 70 mV. In addition to these features, there is a $1e^-$ oxidation of $[\mathbf{Ru}^{II}-OH_2]^{2+}$ to $[\mathbf{Ru}^{III}-OH_2]^{3+}$, a $1e^-/2H^+$ oxidation of $[\mathbf{Ru}^{III}-OH_2]^{3+}$ to $[\mathbf{Ru}^{IV}=O]^{2+}$, a $1e^-$ oxidation of $[\mathbf{Ru}^{IV}=O]^{2+}$ to $[\mathbf{Ru}^{V}=O]^{3+}$, and a $2e^-/2H^+$ oxidation of $[\mathbf{Ru}^{III}-OH_2]^{3+}$ to $[\mathbf{Ru}^{V}=O]^{3+}$. The $[\mathbf{Ru}^{III}-OOH]^{2+}$ intermediate is reached either by the $1e^-/1H^+$ oxidation of $[\mathbf{Ru}^{IV}=O]^{2+}$ involving its reaction with a water molecule coupled to the loss of a proton or the attack of H_2O on $[\mathbf{Ru}^{V}=O]^{3+}$ and the elimination of a proton in a subsequent thermal (nonelectrochemical) reaction. These two oxidations are indicated by dashed lines in Figure 10 in the pH region where the PCET process is predicted to be favored. This thermal step is calculated to be slightly endothermic, and the preceding $1e^-$ oxidation of $[\mathbf{Ru}^{IV}=O]^{2+}$ to $[\mathbf{Ru}^{V}=O]^{3+}$ becomes more and more positive relative to that for the production of $[\mathbf{Ru}^{IV}=O]^{2+}$ with increasing pH. In contrast, the electrochemical conversion of $[\mathbf{Ru}^{IV}=O]^{2+}$ to $[\mathbf{Ru}^{III}-OOH]^{2+}$ is predicted to be possible at all pH values in the diagram and to be favored over the formation of $[\mathbf{Ru}^{V}=O]^{3+}$ at pH above 3.5 (although the calculated position of this PCET potential may be too high). We have also examined the pH dependence of the onset of catalytic current, as shown in Figure S30 (Supporting Information). The onset of background-subtracted catalytic current shows no dependence on pH at low values of pH, then a somewhat complicated behavior as a function of pH between pH 7 and 8.5, and finally an ca. −59 mV/pH dependence at pH > 8.5. Such behavior is consistent with a switchover

Table 2. Standard Reduction Potentials and pK_a Values of Intermediate Species Derived from the Experimental Pourbaix Diagrams

couple	type	E° (V vs NHE)
$[Ru^{III}-OH_2]^{3+}/[Ru^{II}-OH_2]^{2+}$	$1e^-$	1.180
$[Ru^{IV}=O]^{2+}/[Ru^{II}-OH_2]^{2+}$	$2e^-/2H^+$	1.351
$[Ru^{IV}=O]^{2+}/[Ru^{III}-OH_2]^{3+}$	$1e^-/2H^+$	1.523
$[Ru^{V}=O]^{3+}/[Ru^{III}-OH_2]^{3+}$	$2e^-/2H^+$	1.473
$[Ru^{V}=O]^{3+}/[Ru^{IV}=O]^{2+}$	$1e^-$	1.420
$[Ru^{III}-OOH]^{2+}/[Ru^{IV}=O]^{2+}$ [a]	$1e^-/1H^+$	1.621
$[Ru^{IV}-OO]^{2+}/[Ru^{III}-OOH]^{2+}$	$1e^-/1H^+$	0.950
$[Ru^{III}-OOH]^{2+}/[Ru^{II}-OOH]^{+}$	$1e^-$	0.295
$[Ru^{III}-OOH]^{2+}/[Ru^{II}-HOOH]^{2+}$	$1e^-/1H^+$	0.505
$[Ru^{III}-OH_2]^{3+}$	pK_a	2.9
$[Ru^{II}-OOH_2]^{3+}$	pK_a	3.5

[a] Includes theoretical value of 0.201 eV for the standard free energy of the reaction $[Ru^{V}=O]^{3+} + H_2O \rightarrow [Ru^{III}-OOH]^{2+} + H^+$.

from the $Ru^{V}=O$ pathway to a direct pathway involving $Ru^{IV}=O$. The calculated structures of all key intermediates in the proposed catalytic cycles are shown in Figure S31 (Supporting Information). Those of $[Ru^{II}-HOOH]^{2+}$, $[Ru^{II}(NPMH^+)(pic)_2-OOH]^{2+}$, and $[Ru^{II}(NPMH^+)(pic)_2-OH_2]^{3+}$ are shown in Figure S32 (Supporting Information).

Using the experimental standard reduction potentials and pK_a values derived from the Pourbaix diagrams in Figures 2 and 9 and listed in Table 2 and the calculated energetics listed in Table 1, one can construct the experimental and theoretical Latimer–Frost diagrams, as shown in Figure 11 (under standard conditions) and Figure S33 (Supporting Information) (at pH 7). The calculated ΔG^* of the thermal reaction $[Ru^{V}=O]^{3+} + H_2O \rightarrow [Ru^{III}-OOH]^{2+} + H^+$ was used in the experimental diagrams. In these diagrams, the cumulative free energy change relative to the resting state of the catalyst complex, $[Ru^{II}-OH_2]^{2+}$, for producing the various intermediates is plotted as a function of the number of electrons, n, removed in the oxidation process. Any intermediate that lies above the line joining its neighboring points is unstable with respect to disproportionation. The largest vertical distance from the line joining the points corresponding to $n = 0$ and $n = 4$ or $n = 1$ and $n = 5$, corresponding to the thermodynamic 4-electron oxidation potential, to an intermediate represents an intrinsic thermodynamic overpotential of the catalyst for a $0 \rightarrow 4$ cycle or a $1 \rightarrow 5$ cycle, respectively. It is clear from both panels of Figure 11 that in the present case this is associated with the $[Ru^{III}-OOH]^{2+}$ intermediate and lower (only 257 mV in the experimental plot) for the $1 \rightarrow 5$ cycle than for the $0 \rightarrow 4$ cycle. We see no evidence in our experiments or our calculations of the blue lines in Figure 11 that would culminate a $0 \rightarrow 4$ cycle either by direct elimination of $^3O_2$ through the PCET oxidation of $[Ru^{III}-OOH]^{2+}$ or by the decomposition of $[Ru^{IV}-OO]^{2+}$ following the PCET oxidation of $[Ru^{III}-OOH]^{2+}$.

Another interesting aspect of the calculations is that those with the small basis set predict that the sequential PCET steps $[Ru^{II}-OH_2\cdot H_2O]^{2+} \rightarrow [Ru^{III}-OH\cdot H_2O]^{2+}$ and $[Ru^{III}-OH\cdot H_2O]^{2+} \rightarrow [Ru^{IV}=O\cdot H_2O]^{2+}$ should occur as a single two-electron, two-proton step with standard free-energy change 1.06 eV (1.06 V standard reduction potential) as shown in Figure S29 (Supporting Information). On the other hand, the results incorporating a single-point calculation with the large

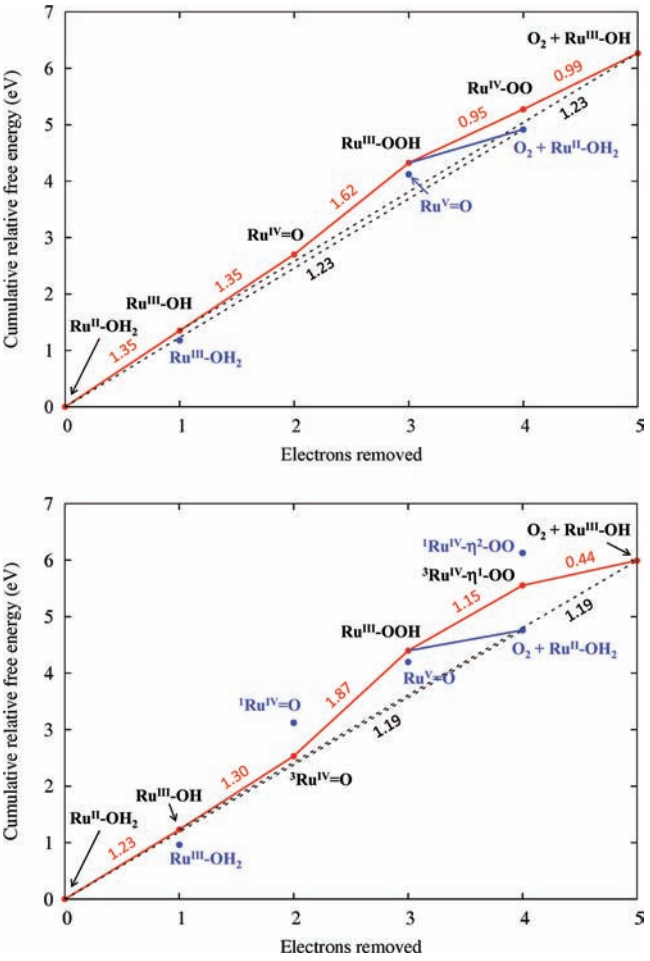

Figure 11. Experimental (top) and theoretical (bottom) Latimer–Frost diagrams for the oxidation of $[Ru^{II}-OH_2]^{2+}$ along the proposed catalytic pathway under standard conditions (i.e., pH 0).

basis predict that the potential for the second step is 70 mV larger than that of the first step (Figure 10). While the difference obtained in the two calculations is certainly within the calculational error, this feature of the results has implications regarding the topology of the Pourbaix diagram.

The oxidation state assignments in intermediates suggested by the calculations are in a few cases unconventional for mononuclear ruthenium oxidation catalyst species. If the assignments were based primarily on the computed spin density distribution in open-shell species and, of course, the relative energetics of singlet and triplet intermediates, they would differ from the conventional ones. The first of the these assignments along the proposed catalytic pathway would be the designation of intermediate $[Ru^{IV}=O\cdot H_2O]^{2+}$ as triplet $[Ru^{IV}=O]^{2+}$ arising from an intermediate spin triplet state at the metal center but having some $^3[Ru^{III}-(O^{\bullet-})]^{2+}$ character as discussed in "Theoretical Characterization of $[Ru^{IV}=O]^{2+}$ and $[Ru^{IV}-OO]^{2+}$" in the Supporting Information. The intermediate $^2[Ru^{V}=O\cdot H_2O]^{3+}$ is assigned conventionally because it would arise from removing an electron from the metal side in either panel of Scheme S4 (Supporting Information), leading to the unpaired electron in the π^* orbital being shared more or less equally between the metal center and oxygen atom and consistent with the computed spin density distribution shown in Figure S10 (Supporting Information).

Scheme 1. Energetics of the Net Reaction $2[Ru^{IV}=O]^{2+} + H_2O \rightarrow [Ru-OH_2]^{2+} + [Ru^{IV}-OO]^{2+}$

$[Ru^{IV}=O]^{2+} \rightarrow [Ru^{V}=O]^{3+} + e^-$, $\Delta G(pH\ 1) = 1.420$ eV

$[Ru^{V}=O]^{3+} + H_2O \rightarrow [Ru^{III}-OOH]^{2+} + H^+$, $\Delta G(pH\ 1) = 0.142$ eV

$[Ru^{III}-OOH]^{2+} \rightarrow [Ru^{IV}-OO]^{2+} + H^+ + e^-$, $\Delta G(pH\ 1) = 0.891$ eV

$[Ru^{IV}=O]^{2+} + 2H^+ + e^- \rightarrow [Ru^{III}-OH_2]^{3+}$, $\Delta G(pH\ 1) = -1.405$ eV

$[Ru^{III}-OH_2]^{3+} + e^- \rightarrow [Ru^{II}-OH_2]^{2+}$, $\Delta G(pH\ 1) = -1.180$ eV

$2\,[Ru^{IV}=O]^{2+} + H_2O \rightarrow [Ru^{II}-OH_2]^{2+} + [Ru^{IV}-OO]^{2+}$, $\Delta G(pH\ 1) = -0.132$ eV

Finally, the present DFT calculations predict that it is the triplet $[Ru^{IV}-\eta^1\text{-}OO]^{2+}$ rather than the singlet $[Ru^{IV}-\eta^2\text{-}OO]^{2+}$ species that results from the $[Ru^{III}-(OOH)\cdot H_2O]^{2+} \rightarrow [Ru^{IV}-(OO)\cdot H_2O]^{2+}$ step, as shown in the lower half of Table S2 and in Scheme S5 (Supporting Information). The singlet $[Ru^{IV}-\eta^2\text{-}OO]^{2+}$ species (i.e., the conformer with the O−O axis approximately in the equatorial plane) is computed to lie 13.2 kcal mol^{-1} higher in standard free energy than the triplet $[Ru^{IV}-\eta^1\text{-}OO]^{2+}$ species, and, like the $^3[Ru^{IV}=O]^{2+}$ species, arises from an intermediate spin triplet Ru(IV) metal center. The spin density distribution of the triplet state (Figure S10, Supporting Information) indicates considerable spin on the two oxygen atoms (and very little spin on the Ru center), which can be accounted for by the two singly occupied molecular orbitals having much more peroxo π^* character than Ru d_π character. The localization of the unpaired spins on the peroxo π^* orbitals imparts strong $[Ru^{II}-\eta^{1\text{-}3}(OO)]^{2+}$ character to this species, consistent with the computed spin density shown in Figure S10 (Supporting Information). Table S2 (Supporting Information) shows that the singlet (η^2) state is stabilized by GVB-CI involving the Ru−O π and (7%) π^* orbitals, similar to the singlet state of $[Ru^{IV}=O]^{2+}$ in trading an intermediate-spin metal center, albeit one with extensive mixing with the O_2^{2-} π^* orbitals, for a low-spin metal center and a vacant π^* orbital available for GVB-CI. Here again, the singlet state is predicted to be stabilized enough by valence configuration interaction to be the ground electronic state. Similar to the case of the triplet η^1 species, the donation of two electrons to orbitals strongly localized on the metal center should impart strong $[Ru^{II}-\eta^{2\text{-}1}(OO)]^{2+}$ character to singlet $[Ru^{IV}-\eta^2\text{-}OO]^{2+}$.

The Ru−O and O−O vibrations are calculated to be 470 cm^{-1} (Ru−O_2 symmetric stretch), 609 cm^{-1} (Ru−O_2 antisymmetric stretch), and 1105 cm^{-1} (O−O stretch) for $^1[Ru^{IV}-\eta^2\text{-}OO]^{2+}$, as opposed to 348 cm^{-1} (Ru−O stretch) and 1352 cm^{-1} (O−O stretch) for the $^3[Ru^{IV}-\eta^1\text{-}OO]^{2+}$ species (see Table S1, Supporting Information). Since the calculated O−O stretches do not match well with experimental data, we investigated $^1[Ru^{IV}-\text{cyc-}OON]^{2+}$ where the O−O interacts with a noncoordinating nitrogen of the NPM ligand. However, this species is energetically 21.88 kcal mol^{-1} higher than $^3[Ru^{IV}-\eta^1\text{-}OO]^{2+}$ (and 8.65 kcal mol^{-1} higher than $^1[Ru^{IV}-\eta^2\text{-}OO]^{2+}$). The calculated spectroscopic properties of this species (absorption max at 500 and 698 nm) are also in disagreement with experimental data.

DISCUSSION

Reactivity of $[Ru^{IV}=O]^{2+}$ in Water (pH 1). The experimental observation that aqueous $[Ru^{IV}=O]^{2+}$ solutions in concentrations higher than ca. 10^{-5} M spontaneously react to form approximately equal amounts of $[Ru^{IV}-OO]^{2+}$ and $[Ru^{II}-OH_2]^{2+}$ can be rationalized in terms of Scheme 1 for the net reaction ($2[Ru^{IV}=O]^{2+} + H_2O \rightarrow [Ru^{IV}-OO]^{2+} + [Ru^{II}-OH_2]^{2+}$). The energetics of the elementary steps leading to the net reaction are taken from Table 2 and show that the overall process is exothermic. In fact, the main route for the formation of $[Ru^{IV}(NNN)(NN)(OO)]^{2+}$ has been previously considered via ($[Ru^{V}=O]^{3+} + H_2O \rightarrow [Ru^{III}-OOH]^{2+} + H^+$ and $[Ru^{III}-OOH]^{2+} \rightarrow [Ru^{IV}-OO]^{2+} + H^+ + e^-$).[30,34,36]

Identity of $[Ru^{IV}-OO]^{2+}$. Resonance Raman and ESI-MS measurements were made on samples prepared by four-electron oxidation of $[Ru^{II}-OH_2]^{2+}$ at pH 6. The $[Ru^{II}-OH_2]^{2+}$ content should be at trace amounts, if present at all. The ESI-MS analysis of the solution used for resonance Raman measurements indicated the presence of a species with m/z = 355 (M/2) and 710 (M−1), which correspond to $[Ru^{IV}-{}^{16}O{}^{16}O]^{2+}$. The sample prepared in $H_2{}^{18}O$ gives m/z = 357 and 714 corresponding to the structure $[Ru^{IV}-{}^{18}O{}^{18}O]^{2+}$. It should be pointed out that Wasylenko et al. observed an ESI-MS signal at m/z 523.15 and assigned it as $[Ru(tpy)(bpy)(OO)]^+$.[36] This is a +1 charged species and not the +2 charged species as they and others proposed in the mechanism of water oxidation (eqs 12 and 13).

$$[Ru^{V}=O]^{3+} + H_2O \rightarrow [Ru^{III}-OOH]^{2+} + H^+ \qquad (12)$$

$$[Ru^{III}-OOH]^{2+} - e^- \rightarrow [Ru^{IV}-OO]^{2+} + H^+ \qquad (13)$$

In fact, when an aqueous solution containing $[Ru^{IV}-{}^{16}O{}^{16}O]^{2+}$ decomposed slowly with the λ_{max} shift from 512 to 580 nm, it produces $[Ru^{IV}-{}^{16}O{}^{16}OH]^+$ with m/z 712 for $[Ru^{II}-OOH]^+$ and m/z 356.5 for $[Ru^{II}-OOH]^+ + H^+$. Therefore, we believe that the species Wasylenko et al. observed to have an ESI-MS signal at m/z 523.15 is likely $[Ru(tpy)(bpy)(OOH)]^+$ (MW 523.54).

While mass spectrometry and Coulomb count experiments suggest the formation of a species corresponding to $[Ru^{IV}-OO]^{2+}$, these experimental data do not provide any insight into the bonding between oxygen atoms within the complex. On the other hand, the resonance Raman spectrum of $[Ru^{IV}-OO]^{2+}$ reveals a new distinct vibration at 547 cm^{-1}, which red-shifts only 12 cm^{-1} upon $^{16}O/^{18}O$ substitution. While the direction of the shift is consistent with the presence of a heavier atom (^{18}O), its magnitude appears to be smaller than is predicted from the simple diatomic oscillator model (27 cm^{-1}). The assignment of this vibration to a metal-oxo stretch ($Ru^{IV}=O$) is unlikely since that is usually observed around 800 cm^{-1} with isotopic shifts in the range of 33−45 cm^{-1} (Table S3, Supporting Information).[89−92] However, the vibrational frequencies of the metal−oxygen bond in metal superoxo or hydroperoxo compounds are reported to be in the 500 cm^{-1} region with small isotopic shifts, e.g., 12−21 cm^{-1}, upon $^{16}O/^{18}O$ substitution (Table S4, Supporting Information).[34,90,93−111] For example, in a study reported by Bakac et al.,[97] the vibrational frequency of the Cr−O bond was observed at 503 cm^{-1} by measuring the resonance Raman spectrum of the η^1-superoxochromium(III) complex, and interestingly, its isotopic shift was only 12 cm^{-1} upon $^{16}O/^{18}O$ substitution. It was proposed that significant coupling of the Cr−O stretch with other vibrational modes (e.g., the Cr−O−O bend) leads to the discrepancy between experiment and the calculation based on a diatomic oscillator model. The frequency corresponding to the O−O vibration in superoxo, peroxo, and hydroperoxo metal complexes is usually observed in the region between 830 and 1200 cm^{-1} showing isotopic shifts between 17 and 68 cm^{-1} (Table S4, Supporting Information).

To our knowledge, there are no single-crystal X-ray diffraction studies on ruthenium complexes with the η^1-OO moiety. We have summarized the O−O vibrational frequency of structurally characterized ruthenium complexes with the η^2-OO moiety in Table S4 (Supporting Information). The O−O stretching frequency of ruthenium complexes with the η^2-OO moiety is in the range of 850−920 cm^{-1} regardless of the formal oxidation state of ruthenium. While some spectral changes are observed for $\nu_{^{16}O-^{16}O}$ in the high-frequency region (750−950 cm^{-1}) upon isotopic substitution for the $[\mathbf{Ru}^{IV}-OO]^{2+}$ species,[112] the definitive identification of the band corresponding to the O−O vibration can be complicated by the strong Raman activity of the ligand vibrational modes and a relatively low Raman intensity of the O−O vibration. It should be noted that the Ru−O and O−O vibrations are calculated to be 470 cm^{-1} (Ru−O_2 symmetric stretch), 609 cm^{-1} (Ru−O_2 antisymmetric stretch), and 1105 cm^{-1} (O−O stretch) for singlet $[\mathbf{Ru}^{IV}-\eta^2\text{-}OO]^{2+}$, as opposed to 221 cm^{-1} (Ru−O stretch) and 1350 cm^{-1} (O−O stretch) for the triplet $[\mathbf{Ru}^{IV}-\eta^1\text{-}OO]^{2+}$ species. These vibrational modes are mixed with other modes in most cases. It is clear that the calculated values for the O−O stretch are not good matches (i.e., no observation of a vibrational frequency shift by isotopic labeling experiments in the region of 1000−1500 cm^{-1}), and it is difficult to predict even the geometry of the M−O_2 moiety. While Concepcion et al. assigned 1015 cm^{-1} as the O−O stretch based on DFT calculations for $[Ru^{IV}(Mebimpy)(bpy)(\eta^2\text{-}OO)]^{2+}$ (Mebimpy = 2,6-bis(benzimidazol-2-yl)pyridine), their assignment was not confirmed by labeling experiments.[34] As seen in Table S4 (Supporting Information), experimental data on M−O−O−M species indicate that O−O stretch frequencies change over quite a wide range (800−1200 cm^{-1}) due to different bond strengths, electron distributions, geometries, etc. Also, any hydrogen bonding of the bound O−O (or OOH) with solvent water molecules and/or interaction with a noncoordinating nitrogen of the NPM ligand may decrease the O−O or M−O stretching frequencies (e.g., see $^1[\mathbf{Ru}^{IV}-cyc\text{-}OON]^{2+}$ in Table 1). The low vibrational frequency (547 cm^{-1}) and small isotopic shift (12 cm^{-1}) for Ru−O of $[\mathbf{Ru}^{IV}-OO]^{2+}$ are reasonable for those of η^1-OO or η^2-OO complexes. The small isotopic shift observed in the Ru−O stretching frequencies for both $[\mathbf{Ru}^{IV}-\eta^1\text{-}OO]^{2+}$ and $[\mathbf{Ru}^{IV}-\eta^2\text{-}OO]^{2+}$ is, however, consistent with our DFT calculations, which indicate that the vibrational modes are mixed with various other modes and, by analogy to the above-mentioned case of Cr−OO, with small isotopic shifts.

Now we discuss the electrochemistry of $[\mathbf{Ru}^{IV}-OO]^{2+}$. A sample was prepared by bulk electrolysis (four-electron oxidation of $[\mathbf{Ru}^{II}-OH_2]^{2+}$) at pH 6, and the electrochemical data shown in the bottom panel of Figure 8 were taken after performing resonance Raman and ESI-MS measurements. Currents were observed at potentials corresponding to the red and blue lines, but not the green line, in Figure 9 during both anodic and cathodic scans. However, the cathodic scan starting at 1240 mV of $[\mathbf{Ru}^{II}-OH_2]^{2+}$ led to the formation of a new species that has reduction potentials at the blue and green lines in Figure 9. Eventually, after repeated scans, another species that has a reduction potential at the red line started to be observed. These results suggest the existence of geometric isomers for $[\mathbf{Ru}^{IV}-OO]^{2+}$. We tentatively assigned the electrochemically prepared sample used for the resonance Raman measurement to be $[\mathbf{Ru}^{IV}-\eta^2\text{-}OO]^{2+}$. When the $[\mathbf{Ru}^{IV}-\eta^2\text{-}OO]^{2+}$ species is reduced, protonation of one of the O atoms may take place while retaining (at least during the voltammetric time scale) the η^2 configuration. The species $[\mathbf{Ru}^{IV}-\eta^2\text{-}OOH]^{2+}$ does not seem to reduce to $[\mathbf{Ru}^{IV}-\eta^2\text{-}OOH]^{+}$ or $[\mathbf{Ru}^{IV}-\eta^2\text{-}HOOH]^{2+}$ at potentials greater than 100 mV. At an applied potential at 1240 mV, $[\mathbf{Ru}^{III}-OOH]^{2+}$ is produced, which is reduced to $[\mathbf{Ru}^{II}-OOH]^{+}$ and $[\mathbf{Ru}^{II}-HOOH]^{2+}$ at the potential of the green line in Figure 9. Once the produced $[\mathbf{Ru}^{III}-OOH]^{2+}$ is further oxidized at 1240 mV, $[\mathbf{Ru}^{IV}-\eta^1\text{-}OO]^{2+}$ likely forms and may eventually convert to $[\mathbf{Ru}^{IV}-\eta^2\text{-}OO]^{2+}$. While a pendent base on the NPM ligand could possibly be involved in the above reactions via a hydrogen bonding interaction with the OOH moiety, we do not have any clear evidence of it, and our DFT calculations indicate otherwise.

In conclusion, we have assigned this species as $^1[\mathbf{Ru}^{IV}-\eta^2\text{-}OO]^{2+}$ based on electrochemical, spectroscopic, and theoretical plausibility alongside a previously published conclusion by the T. J. Meyer's group[34] and an X-ray structural database for Ru−OO species, although there remains some conflicting evidence, especially the higher energy of $^1[\mathbf{Ru}^{IV}-\eta^2\text{-}OO]^{2+}$ compared to $^3[\mathbf{Ru}^{IV}-\eta^1\text{-}OO]^{2+}$ predicted by DFT and BS-DFT, but not by CASSCF calculations.

Oxygen Release from $[\mathbf{Ru}^{IV}-OO]^{2+}$. Despite the fact that the formation of the O−O bond is achieved at relatively low potentials via reaction of an $[\mathbf{Ru}^{V}=O]^{3+}$ or $[\mathbf{Ru}^{IV}=O]^{2+}$ complex, the oxygen molecule remains bound to the Ru center in $[\mathbf{Ru}^{IV}-OO]^{2+}$ and requires an additional oxidation to be liberated into solution. This unusual stability of $[\mathbf{Ru}^{IV}-OO]^{2+}$ is evident from the fact that, if left in solution, $[\mathbf{Ru}^{IV}-OO]^{2+}$ was slowly reduced to form $[\mathbf{Ru}^{II}-OOH]^{+}$. However, the addition of Ce(IV) to $[\mathbf{Ru}-OO]^{2+}$ results in oxygen evolution. On the other hand, the oxygen evolution from an analogue of $[\mathbf{Ru}^{IV}-OO]^{2+}$ reported by Meyer's group[34] occurs thermally, but very slowly ($k = 7.5 \times 10^{-4}\ s^{-1}$). This thermal process could involve conversion to the triplet $[\mathbf{Ru}^{IV}-\eta^1\text{-}OO]^{2+}$ state as a first step, followed by displacement of triplet O_2 by a water molecule to form singlet $[\mathbf{Ru}^{II}-OH_2]^{2+}$, in a manner analogous to that indicated by the blue lines in both the experimental and theoretical Latimer−Frost diagrams of Figure 11. This reaction was found to be accelerated by several orders of magnitude upon additional oxidation of $[\mathbf{Ru}^{IV}-OO]^{2+}$. The reactivity of the singlet $[\mathbf{Ru}^{IV}-OO]^{2+}$ complex is similar to that in one branch of a previously proposed mechanism of its analogue studied by Meyer's group,[34] i.e., sequential or concurrent oxidation and addition of H_2O with loss of a proton and elimination of triplet O_2. The additional oxidation of $[\mathbf{Ru}^{IV}-OO]^{2+}$ apparently lowers the kinetic barrier for O_2 release and returns the catalyst not to its original $[\mathbf{Ru}^{II}-OH_2]^{2+}$ state but rather to the one-electron-oxidized $[\mathbf{Ru}^{III}-OH]^{2+}$ intermediate.

Identity of $[\mathbf{Ru}^{IV}=O]^{2+}$. There have been extensive studies on $Ru^{IV}=O$ species that display the triplet spin state[82−87] but are not $[\mathbf{Ru}^{III}-O^{\bullet-}]^{2+}$. NMR spectra of $[Ru^{IV}(tpy)(bpy)(O)]^{2+}$ in D_2O and $[\mathbf{Ru}^{IV}=O]^{2+}$ in CD_3CN indicate that these complexes exhibit typical triplet spectra (Figures S13 and S14, Supporting Information). It is of interest that $[Ru^{IV}(tpy)(bpy)(O)]^{2+}$ is stable in water (pH 1), but $[\mathbf{Ru}^{IV}=O]^{2+}$ decomposes to $[\mathbf{Ru}^{IV}-OO]^{2+}$ and $[\mathbf{Ru}^{II}-OH_2]^{2+}$ in 2 h. While the role of a pendent base of the NPM ligand is not clear in this reaction, the Ru^V/Ru^{IV} potential is almost 400 mV less positive than that of $[Ru^{IV}(tpy)(bpy)(O)]^{2+}$, indicating that the $[\mathbf{Ru}^{V}=O]^{3+}$ species might easily form.

Mechanism of Formation of $[\mathbf{Ru}^{IV}-OO]^{2+}$. The proposed cycle for the water oxidation reaction catalyzed by $[\mathbf{Ru}^{II}-OH_2]^{2+}$ is shown in Figure 12. The main focus of the discussion will be on the crucial step of O−O bond formation and the identity of the $[\mathbf{Ru}^{IV}-OO]^{2+}$ species.

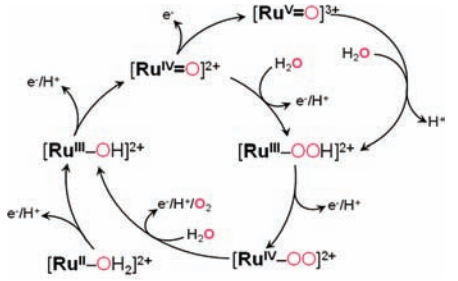

Figure 12. Proposed catalytic cycle of water oxidation reaction catalyzed by $[Ru^{II}-OH_2]^{2+}$.

The proposed mechanism assumes that the formation of the O−O bond may take place either by nucleophilic attack of a water molecule on $[\mathbf{Ru}^{V}{=}O]^{3+}$ (eq 12), as proposed for other mononuclear ruthenium catalysts reported previously,[34,50] or through the reaction of $[\mathbf{Ru}^{IV}{=}O]^{2+}$ with a water molecule and concomitant removal of an electron and a proton (eq 9, the so-called "direct pathway").

The thermodynamics of both oxidation reactions of $[\mathbf{Ru}^{IV}{=}O]^{2+}$ were predicted theoretically (Figure 10 and Table 1), and it was found that the formation of $[\mathbf{Ru}^{V}{=}O]^{3+}$ (eq 5) at standard conditions (pH 0) requires a lower applied potential compared to the direct pathway. The subsequent addition of a water molecule to $[\mathbf{Ru}^{V}{=}O]^{3+}$ (eq 12) is, however, a thermodynamically slightly uphill reaction requiring an additional 4.64 kcal mol^{-1} under standard conditions (Table 1). Given that the concentration of the water reactant in that thermal reaction is 55.4 M, the reaction should proceed fairly well. At standard conditions, the net change in free energy is the same for the direct pathway (eq 9) and the formation of $[\mathbf{Ru}^{V}{=}O]^{3+}$ followed by the addition of water (eq 5 + eq 12). However, in the high pH region the direct pathway becomes more energetically favorable compared to the formation of $[\mathbf{Ru}^{V}{=}O]^{3+}$ since the former is a proton-coupled reaction and the latter is not (Figure 12). An analysis of the experimental Latimer−Frost diagram at pH 7 indicates that generation of $[\mathbf{Ru}^{V}{=}O]^{3+}$ from $[\mathbf{Ru}^{IV}{=}O]^{2+}$ is more endothermic, compared to the "direct pathway" to produce $[\mathbf{Ru}^{III}{-}OOH]^{2+}$ (Figure S33, Supporting Information). The possible "branching" of the mechanism at Ru^{IV} and Ru^{V} oxo species was suggested by Berlinguette[36] based on a kinetic analysis of spectroscopically observed intermediates and the overall catalytic rate of O_2 production. These multiple pathways become easily accessible since powerful oxidants such as Ce(IV) are used to drive these reactions.

For example, consider the bulk electrolysis experiments at pH 1 with an applied potential of 1260 mV, and at pH 6 with an applied potential of 1150 mV, i.e., 160 and 270 mV below the 1420 mV of the $\mathbf{Ru}^{V}{=}O/\mathbf{Ru}^{IV}{=}O$ couple, respectively. From the Nernst equation for the one-electron reduction of $[\mathbf{Ru}^{V}{=}O]^{3+}$, we obtain $[\mathbf{Ru}^{V}{=}O^{3+}]/[\mathbf{Ru}^{IV}{=}O^{2+}] = \exp((E_i - E^{\circ})/RT) \equiv f_i$ under the experimental conditions at pH "*i*". The subsequent reaction of nucleophilic attack by a water molecule on $[\mathbf{Ru}^{V}{=}O]^{3+}$ (eq 12) for a similar mononuclear ruthenium complex was estimated by Concepcion et al.[34] to have a pseudo first-order rate constant, k_{O-O}, of 9.6×10^{-3} s^{-1}. Assuming a rapid pre-equilibrium and neglecting the back reaction of $[\mathbf{Ru}^{III}{-}OOH]^{2+}$, both assumptions favoring the production of $[\mathbf{Ru}^{III}{-}OOH]^{2+}$ through the $[\mathbf{Ru}^{V}{=}O]^{3+}$ route, the effective pseudo first-order rate constant for the conversion of $[\mathbf{Ru}^{IV}{=}O]^{2+}$ to $[\mathbf{Ru}^{III}{-}OOH]^{2+}$ becomes $k_{eff} = k_{O-O} \times f_i$, so that the $1/e$ time for conversion under the experimental conditions at pH "*i*" should be $\tau_i = 1/(k_{O-O} \times f_i)$. Under the conditions of the underpotential bulk electrolysis at pH 1 and 6, $f_1 = 2.0 \times 10^{-3}$ and $f_6 = 2.7 \times 10^{-5}$. This gives $\tau_1 = 15$ h and $\tau_6 = 1100$ h, both negligibly slow compared to the experimental time scale (20−40 min). However, if k_{O-O} were 2 orders of magnitude faster than that estimated by Concepcion et al., $\tau_1 = 8.7$ min and $\tau_6 = 11$ h. The shorter value of τ_1 appears to be of the same order as the experimental time scale for underpotential electrolysis; however, τ_6 still remains too large. While this experimental observation and the background-subtracted onset of catalytic current of $[\mathbf{Ru}^{II}{-}OH_2]^{2+}$ at various pH (Figure S30, Supporting Information) do not offer definitive proof of the "direct route", it demonstrates that $[\mathbf{Ru}^{III}{-}OOH]^{2+}$ can be formed in large part by some pathway that does not involve $[\mathbf{Ru}^{V}{=}O]^{3+}$. Any reactions involving direct interactions with the ceric ammonium salt, as proposed for other systems,[36] can be dismissed in our case since no cerium was used in the electrolysis experiments.

There is as of yet no clear understanding of the exact mechanism for the direct pathway. An early theoretical study by Wang et al.[113] demonstrated that formation of an O−O bond at a Ru^{IV} center is unfavorable; however, later experimental studies have proposed that $[Ru^{IV}(tpy)(bpy)(O)]^{2+}$ can react with a water molecule to yield $[Ru^{II}(tpy)(bpy)(H_2O_2)]^{2+}$.[36] We do not have strong experimental evidence for such a reaction except that: (1) two molecules of $[\mathbf{Ru}^{IV}{=}O]^{2+}$ convert completely to $[\mathbf{Ru}^{IV}{-}OO]^{2+}$ and $[\mathbf{Ru}^{II}{-}OH_2]^{2+}$ in less than 2 h (i.e., the reactions via $[\mathbf{Ru}^{V}{=}O]^{3+}$ seem too slow as mentioned above); (2) the observation of m/z 356.9 that corresponds to $[\mathbf{Ru}^{II}{-}HOOH]^{2+}$ (or $[\mathbf{Ru}^{IV}{=}O\cdots H_2]^{2+}$); and (3) the onset of background-subtracted catalytic current in CV scans shows a change in pH dependence from low values of pH to higher values, with an ca. −59 mV/pH dependence at pH > 8.5, consistent with a switchover from the $[\mathbf{Ru}^{V}{=}O]^{3+}$ pathway to a direct pathway involving $[\mathbf{Ru}^{IV}{=}O]^{2+}$. We assume that an equilibrium concentration of a $[\mathbf{Ru}^{IV}{=}O\cdots H_2O]^{2+}$ complex can exist in solution with a water molecule in close proximity to the Ru center, which can be further oxidized and deprotonated to form an O−O bonded species.

Finally, the proposed $[\mathbf{Ru}^{IV}{-}\eta^1\text{-}OOH]^{2+}$ (Figure 12) was not observed, probably due to facile proton-coupled oxidation to form $[\mathbf{Ru}^{IV}{-}\eta^1\text{-}OO]^{2+}$ and possibly further conversion to $[\mathbf{Ru}^{IV}{-}\eta^2\text{-}OO]^{2+}$. However, the puzzle that the lowest-energy state found from DFT calculations corresponds to a $[\mathbf{Ru}^{IV}{-}\eta^1\text{-}OO]^{2+}$ complex still remains. CASSCF calculations favor the $[\mathbf{Ru}^{IV}{-}\eta^2\text{-}OO]^{2+}$ state, but because their energies do not reflect the dynamic correlation included in the DFT calculations, they are only semiquantative. Do state-of-the-art calculations have limitations in predicting the energetics, spin densities, and vibrational properties of $[\mathbf{Ru}^{IV}{-}OO]^{2+}$ species?

■ CONCLUSIONS

This study describes the characterization of intermediates in water oxidation catalyzed by a mononuclear ruthenium complex containing a dinaphthyridyl pyridine ligand having two basic sites not directly bound to the metal center. Electrochemistry, UV−vis and resonance Raman spectroscopy, pulse radiolysis, stopped flow, and ESI-MS with $H_2{}^{18}O$ labeling experiments, and theoretical calculations were collectively used to identify the electronic, spectroscopic, and structural properties of intermediates. The results reveal a number of intriguing properties of intermediates such as $[\mathbf{Ru}^{IV}{=}O]^{2+}$ and $[\mathbf{Ru}^{IV}{-}OO]^{2+}$.

The key findings are the following:

(a) The potential of the $[Ru^{III}-OH]^{2+}/[Ru^{II}-OH_2]^{2+}$ couple is equal to or higher than the potential of the $[Ru^{IV}=O]^{2+}/[Ru^{II}-OH]^{2+}$ couple. The rate constant of the first oxidation by Ce(IV) is $(2.0 \pm 0.3) \times 10^4\ M^{-1}\ s^{-1}$ (at pH 1).

(b) At pH 1 both $[Ru^{IV}=O]^{2+}$ and $[Ru^{V}=O]^{3+}$ exist in equilibrium in a ratio of ca. 1:1.

(c) The formation of $[Ru^{III}-OOH]^{2+}$ can proceed via formation of $[Ru^{V}=O]^{3+}$ followed by nucleophilic attack by a water molecule at pH < 1; however, this pathway cannot account for the product formation at pH 6. An alternative pathway was proposed for the reaction of $[Ru^{IV}=O]^{2+}$ with a water molecule accompanied by the concomitant removal of an electron and a proton ("direct pathway"). The direct pathway (or some other as of yet unidentified pathway) becomes predominant at higher pH in underpotential bulk electrolysis experiments and in the onset of catalytic current in background-subtracted CV scans as a function of pH.

(d) While there remains some conflicting evidence, the Ru−OO species is most likely $^1[Ru^{IV}-\eta^2\text{-}OO]^{2+}$ based on our electrochemical, spectroscopic, and theoretical data alongside a previously published conclusion by T. J. Meyer's group.[34]

(e) $[Ru^{IV}-OO]^{2+}$ slowly transforms to $[Ru^{II}-OOH]^{+}$ without releasing oxygen, but in the presence of additional Ce(IV) oxidant, $[Ru^{IV}-OO]^{2+}$ yields O_2.

■ ASSOCIATED CONTENT

Supporting Information. CV of $[Ru^{II}-OH_2]^{2+}$ (pH 1); spectral changes of $[Ru^{II}-OH_2]^{2+}$ upon Ce(IV) titration; [Ce(IV)] dependence of disappearance of $[Ru^{II}-OH_2]^{2+}$; kinetic data for the reaction of $[Ru^{II}-OH_2]^{2+}$ with the carbonate radical; calculated UV−vis spectra for $^1[Ru^{IV}=O]^{2+}$, $^3[Ru^{IV}=O]^{2+}$, $[Ru^{II}-OH_2]^{2+}$, $[Ru^{IV}-\eta^1\text{-}OO]^{2+}$, and $[Ru^{IV}-\eta^2\text{-}OO]^{2+}$; active space orbitals and orbital populations for $^1[Ru^{IV}=O]^{2+}$, $^3[Ru^{IV}=O]^{2+}$, $^3[Ru^{IV}-\eta^1\text{-}OO]^{2+}$, and $^1[Ru^{IV}-\eta^2-OO]^{2+}$; computed spin densities for $^3[Ru^{IV}=O]^{2+}$, $^2[Ru^{V}=O]^{3+}$, and $^3[Ru^{IV}-OO]^{2+}$; observed spectra for $[Ru^{IV}=O]^{2+}$ at pH 1 and 10; NMR spectrum of the solution containing $[Ru^{IV}-OO]^{2+}$, $[Ru^{IV}=O]^{2+}$, and $[Ru^{IV}(tpy)(bpy)O]^{2+}$; CV of $[Ru^{IV}=O]^{2+}$ in CH_3CN; ESI-MS of $[Ru^{IV}-OO]^{2+}$ prepared in $H_2{}^{16}O$ and $H_2{}^{18}O$; resonance Raman spectra of $[Ru^{II}-OH_2]^{2+}$ and $[Ru^{IV}-OO]^{2+}$; ESI-MS of the reaction mixture after addition of Ce(IV); ESI-MS and NMR spectra of $[Ru^{II}-OOH]^{+}$; calculated Pourbaix diagram; CV scans showing onset of background-corrected catalytic current vs pH; calculated structures of key intermediates; experimental Latimer−Frost diagram at pH 7; theoretical characterization of $[Ru^{IV}=O]^{2+}$ and $[Ru^{IV}-OO]^{2+}$; details of calculated electrochemistry in aqueous solution; several thermodynamic cycles; schematic frontier orbital diagrams; table of calculated energies of $[Ru^{IV}=O\cdot H_2O]^{2+}$ and $[Ru^{IV}-(OO)\cdot H_2O]^{2+}$; three tables for vibrational frequencies and their isotopic shifts of M=O, M−O, and O−O bonds; calculated Cartesian coordinates of key intermediates in water oxidation catalysis by $[Ru^{II}-(OH_2)(H_2O)]^{2+}$; and the complete ref 53. This material is available free of charge via the Internet at http://pubs.acs.org.

■ AUTHOR INFORMATION

Corresponding Author
dep@bnl.gov; fujita@bnl.gov

Present Addresses
[§]Department of Chemistry, University of Massachusetts, Boston, MA 02125.

■ ACKNOWLEDGMENT

We thank Dr. Norman Sutin and Dr. Carol Creutz for helpful discussions. The work at Brookhaven National Laboratory (BNL) is funded under contract DE-AC02-98CH10886, and the work at Houston is funded under contract DE-FG02-07ER15888 with the U.S. Department of Energy and supported by its Division of Chemical Sciences, Geosciences, & Biosciences, Office of Basic Energy Sciences. The BNL authors also thank the U.S. Department of Energy for funding under the BES Hydrogen Fuel Initiative. RZ and RPT also thank the Robert A. Welch Foundation (E-621).

■ REFERENCES

(1) Eisenberg, R.; Nocera, D. G. *Inorg. Chem.* **2005**, *44*, 6799–6801.
(2) Lewis, N. S.; Nocera, D. G. *Proc. Natl. Acad. Sci. U.S.A.* **2006**, *103*, 15729–15735.
(3) Alstrum-Acevedo, J. H.; Brennaman, M. K.; Meyer, T. J. *Inorg. Chem.* **2005**, *44*, 6802–6827.
(4) Brimblecombe, R.; Dismukes, G. C.; Swiegers, G. F.; Spiccia, L. *Dalton Trans.* **2009**, 9374–9384.
(5) Huynh, M. H.; Meyer, T. J. *Chem. Rev.* **2007**, *107*, 5004–5064.
(6) Eisenberg, R.; Gray, H. B. *Inorg. Chem.* **2008**, *47*, 1697–1699.
(7) Balzani, V.; Credi, A.; Venturi, M. *ChemSusChem* **2008**, *1*, 26–58.
(8) Youngblood, W. J.; Lee, S. H. A.; Maeda, K.; Mallouk, T. E. *Acc. Chem. Res.* **2009**, *42*, 1966–1973.
(9) Cook, T. R.; Dogutan, D. K.; Reece, S. Y.; Surendranath, Y.; Teets, T. S.; Nocera, D. G. *Chem. Rev.* **2010**, *110*, 6474–6502.
(10) Walter, M. G.; Warren, E. L.; McKone, J. R.; Boettcher, S. W.; Mi, Q. X.; Santori, E. A.; Lewis, N. S. *Chem. Rev.* **2010**, *110*, 6446–6473.
(11) Dau, H.; Zaharieva, I. *Acc. Chem. Res.* **2009**, *42*, 1861–1870.
(12) Dau, H.; Limberg, C.; Reier, T.; Risch, M.; Roggan, S.; Strasser, P. *ChemCatChem* **2010**, *2*, 724–761.
(13) Ghosh, P. K.; Brunschwig, B. S.; Chou, M.; Creutz, C.; Sutin, N. *J. Am. Chem. Soc.* **1984**, *106*, 4772–4783.
(14) Ruttinger, W.; Dismukes, G. C. *Chem. Rev.* **1997**, *97*, 1–24.
(15) Gersten, S. W.; Samuels, G. J.; Meyer, T. J. *J. Am. Chem. Soc.* **1982**, *104*, 4029–4030.
(16) Yagi, M.; Kaneko, M. *Chem. Rev.* **2001**, *101*, 21–35.
(17) Wada, T.; Tsuge, K.; Tanaka, K. *Inorg. Chem.* **2001**, *40*, 329–337.
(18) Sens, C.; Romero, I.; Rodriguez, M.; Llobet, A.; Parella, T.; Benet-Buchholz, J. *J. Am. Chem. Soc.* **2004**, *126*, 7798–7799.
(19) Hurst, J. K. *Coord. Chem. Rev.* **2005**, *249*, 313–328.
(20) Muckerman, J. T.; Polyansky, D. E.; Wada, T.; Tanaka, K.; Fujita, E. *Inorg. Chem.* **2008**, *47*, 1787–1802.
(21) Cape, J. L.; Siems, W. F.; Hurst, J. K. *Inorg. Chem.* **2009**, *48*, 8729–8735.
(22) Bozoglian, F.; Romain, S.; Ertem, M. Z.; Todorova, T. K.; Sens, C.; Mola, J.; Rodriguez, M.; Romero, I.; Benet-Buchholz, J.; Fontrodona, X.; Cramer, C. J.; Gagliardi, L.; Llobet, A. *J. Am. Chem. Soc.* **2009**, *131*, 15176–15187.
(23) Xu, Y. H.; Akermark, T.; Gyollai, V.; Zou, D. P.; Eriksson, L.; Duan, L. L.; Zhang, R.; Akermark, B.; Sun, L. C. *Inorg. Chem.* **2009**, *48*, 2717–2719.
(24) Concepcion, J. J.; Jurss, J. W.; Brennaman, M. K.; Hoertz, P. G.; Patrocinio, A. O. T.; Iha, N. Y. M.; Templeton, J. L.; Meyer, T. J. *Acc. Chem. Res.* **2009**, *42*, 1954–1965.
(25) Duan, L. L.; Fischer, A.; Xu, Y. H.; Sun, L. C. *J. Am. Chem. Soc.* **2009**, *131*, 10397–10399.
(26) Jurss, J. W.; Concepcion, J. C.; Norris, M. R.; Templeton, J. L.; Meyer, T. J. *Inorg. Chem.* **2010**, *49*, 3980–3982.

(27) Wasylenko, D. J.; Ganesamoorthy, C.; Koivisto, B. D.; Berlinguette, C. P. *Eur. J. Inorg. Chem.* **2010**, 3135–3142.
(28) Zong, R.; Thummel, R. P. *J. Am. Chem. Soc.* **2005**, *127*, 12802–12803.
(29) Tseng, H. W.; Zong, R.; Muckerman, J. T.; Thummel, R. *Inorg. Chem.* **2008**, *47*, 11763–11773.
(30) Concepcion, J. J.; Jurss, J. W.; Templeton, J. L.; Meyer, T. J. *J. Am. Chem. Soc.* **2008**, *130*, 16462–16463.
(31) McDaniel, N. D.; Coughlin, F. J.; Tinker, L. L.; Bernhard, S. *J. Am. Chem. Soc.* **2008**, *130*, 210–217.
(32) Masaoka, S.; Sakai, K. *Chem. Lett.* **2009**, *38*, 182–183.
(33) Hull, J. F.; Balcells, D.; Blakemore, J. D.; Incarvito, C. D.; Eisenstein, O.; Brudvig, G. W.; Crabtree, R. H. *J. Am. Chem. Soc.* **2009**, *131*, 8730–8731.
(34) Concepcion, J. J.; Tsai, M. K.; Muckerman, J. T.; Meyer, T. J. *J. Am. Chem. Soc.* **2010**, *132*, 1545–1557.
(35) Wasylenko, D. J.; Ganesamoorthy, C.; Koivisto, B. D.; Henderson, M. A.; Berlinguette, C. P. *Inorg. Chem.* **2010**, *49*, 2202–2209.
(36) Wasylenko, D. J.; Ganesamoorthy, C.; Henderson, M. A.; Koivisto, B. D.; Berlinguette, C. P. *J. Am. Chem. Soc.* **2010**, *132*, 16094–16106.
(37) Kanan, M. W.; Nocera, D. G. *Science* **2008**, *321*, 1072–1075.
(38) Romain, S.; Vigara, L.; Llobet, A. *Acc. Chem. Res.* **2009**, *42*, 1944–1953.
(39) Sartorel, A.; Miro, P.; Salvadori, E.; Romain, S.; Carraro, M.; Scorrano, G.; Di Valentin, M.; Llobet, A.; Bo, C.; Bonchio, M. *J. Am. Chem. Soc.* **2009**, *131*, 16051–16053.
(40) Geletii, Y. V.; Botar, B.; Koegerler, P.; Hillesheim, D. A.; Musaev, D. G.; Hill, C. L. *Angew. Chem., Int. Ed.* **2008**, *47*, 3896–3899.
(41) Geletii, Y. V.; Huang, Z. Q.; Hou, Y.; Musaev, D. G.; Lian, T. Q.; Hill, C. L. *J. Am. Chem. Soc.* **2009**, *131*, 7522–7523.
(42) Sala, X.; Romero, I.; Rodriguez, M.; Escriche, L.; Llobet, A. *Angew. Chem., Int. Ed.* **2009**, *48*, 2842–2852.
(43) Romero, I.; Rodriguez, M.; Sens, C.; Mola, J.; Kollipara, M. R.; Francas, L.; Mas-Marza, E.; Escriche, L.; Llobet, A. *Inorg. Chem.* **2008**, *47*, 1824–1834.
(44) Duan, L.; Xu, Y.; Zhang, P.; Wang, M.; Sun, L. *Inorg. Chem.* **2009**, *49*, 209–215.
(45) Duan, L.; Xu, Y. H.; Gorlov, M.; Tong, L. P.; Andersson, S.; Sun, L. C. *Chem.—Eur. J.* **2010**, *16*, 4659–4668.
(46) Nyhlen, J.; Duan, L. L.; Akermark, B.; Sun, L. C.; Privalov, T. *Angew. Chem., Int. Ed.* **2010**, *49*, 1773–1777.
(47) Zhang, G.; Zong, R.; Tseng, H.-W.; Thummel, R. P. *Inorg. Chem.* **2008**, *47*, 990–998.
(48) Takeuchi, K. J.; Thompson, M. S.; Pipes, D. W.; Meyer, T. J. *Inorg. Chem.* **1984**, *23*, 1845–1851.
(49) Concepcion, J. J.; Jurss, J. W.; Norris, M. R.; Chen, Z. F.; Templeton, J. L.; Meyer, T. J. *Inorg. Chem.* **2010**, *49*, 1277–1279.
(50) Chen, Z. F.; Concepcion, J. J.; Hu, X. Q.; Yang, W. T.; Hoertz, P. G.; Meyer, T. J. *Proc. Natl. Acad. Sci. U.S.A.* **2010**, *107*, 7225–7229.
(51) Chen, Z. F.; Concepcion, J. J.; Hull, J. F.; Hoertz, P. G.; Meyer, T. J. *Dalton Trans* **2010**, *39*, 6950–6952.
(52) Zanello, P. *Inorganic Electrochemistry. Theory, Practice and Application*; The Royal Society of Chemistry: Cambridge, 2003.
(53) *Gaussian09*, revision B.01; Gaussian, Inc.: Wallingford, CT, 2009 (see SI for complete reference).
(54) Becke, A. D. *Phys. Rev. A* **1988**, *38*, 3098–3100.
(55) Lee, C. T.; Yang, W. T.; Parr, R. G. *Phys. Rev. B* **1988**, *37*, 785–789.
(56) Vosko, S. H.; Wilk, L.; Nusair, M. *Can. J. Phys.* **1980**, *58*, 1200–1211.
(57) Becke, A. D. *J. Chem. Phys.* **1993**, *98*, 5648–5652.
(58) Stephens, P. J.; Devlin, F. J.; Chabalowski, C. F.; Frisch, M. J. *J. Phys. Chem.* **1994**, *98*, 11623–11627.
(59) Andrae, D.; Haeussermann, U.; Dolg, M.; Stoll, H. *Preuss. Theor. Chim. Acta* **1990**, *77*, 123–141.
(60) Martin, J. M. L.; Sundermann, A. *J. Chem. Phys.* **2001**, *114*, 3408–3420.
(61) McLean, A. D.; Chandler, G. S. *J. Chem. Phys.* **1980**, *72*, 5639–5648.
(62) Raghavachari, K.; Binkley, J. S.; Seeger, R.; Pople, J. A. *J. Chem. Phys.* **1980**, *72*, 650–654.
(63) Ditchfield, R.; Hehre, W. J.; Pople, J. A. *J. Chem. Phys.* **1971**, *54*, 724.
(64) Hehre, W. J.; Ditchfield, R.; Pople, J. A. *J. Chem. Phys.* **1972**, *56*, 2257–2261.
(65) Hariharan, P. C.; Pople, J. A. *Theor. Chem. Acc.* **1973**, *28*, 213–222.
(66) Hariharan, P. C.; Pople, J. A. *Mol. Phys.* **1974**, *27*, 209–214.
(67) Gordon, M. S. *Chem. Phys. Lett.* **1980**, *76*, 163–168.
(68) Francl, M. M.; Pietro, W. J.; Hehre, W. J.; Binkley, J. S.; DeFrees, D. J.; Pople, J. A.; Gordon, M. S. *J. Chem. Phys.* **1982**, *77*, 3654–3665.
(69) Barone, V.; Cossi, M. *J. Phys. Chem. A* **1998**, *102*, 1995–2001.
(70) Cossi, M.; Rega, N.; Scalmani, G.; Barone, V. *J. Comput. Chem.* **2003**, *24*, 669–681.
(71) Klamt, A.; Schüürmann, G. *J. Chem. Soc., Perkin Trans. 2* **1993**, 799–805.
(72) Wadsworth, E.; Duke, F. R.; Goetz, C. A. *Anal. Chem.* **1957**, *29*, 1824–1825.
(73) Bishop, E.; Cofre, P. *Analyst* **1981**, *106*, 316–322.
(74) Bondareva, T. N.; Stromberg, A. G. *Zh. Obshch. Khim.* **1955**, *25*, 666–671.
(75) Maverick, A. W.; Yao, Q. *Inorg. Chem.* **1993**, *32*, 5626–5628.
(76) Masllorens, E.; Rodriguez, M.; Romero, I.; Roglans, A.; Parella, T.; Benet-Buchholz, J.; Poyatos, M.; Llobet, A. *J. Am. Chem. Soc.* **2006**, *128*, 5306–5307.
(77) Yoshida, M.; Masaoka, S.; Abe, J.; Sakai, K. *Chem.--Asian J.* **2010**, *5*, 2369–2378.
(78) Huie, R. E.; Clifton, C. L.; Neta, P. *Int. J. Radiat. Appl. Instrum. Part C* **1991**, *38*, 477–481.
(79) The numerical integration feature is a part of the PRWin software package developed at BNL for data aquisition and analysis of pulse radiolysis data.
(80) Chen, S.-N.; Cope, V. W.; Hoffman, M. Z. *J. Phys. Chem.* **1973**, *77*, 1111–1116.
(81) Weeks, J. L.; Rabani, J. *J. Phys. Chem.* **1966**, *70*, 2100–2106.
(82) Moyer, B. A.; Meyer, T. J. *Inorg. Chem.* **1981**, *20*, 436–444.
(83) Dobson, J. C.; Seok, W. K.; Meyer, T. J. *Inorg. Chem.* **1986**, *25*, 1513–1514.
(84) Roecker, L.; Meyer, J. *J. Am. Chem. Soc.* **1987**, *109*, 746–754.
(85) Che, C.-M.; Tang, W.-T.; Wong, W.-T.; Lai, T.-F. *J. Am. Chem. Soc.* **1989**, *111*, 9048–9056.
(86) Che, C.-M.; Yam, V. W. W. *J. Am. Chem. Soc.* **1987**, *109*, 1262–1263.
(87) Benet-Buchholz, J.; Comba, P.; Llobet, A.; Roeser, S.; Vadivelu, P.; Wadepohl, H.; Wiesner, S. *Dalton Trans.* **2009**, 5910–5923.
(88) Kojima, T.; Hirai, Y.; Ishizuka, T.; Shiota, Y.; Yoshizawa, K.; Ikemura, K.; Ogura, T.; Fukuzumi, S. *Angew. Chem., Int. Ed.* **2010**, *49*, 8449–8453.
(89) Yamada, H.; Koike, T.; Hurst, J. K. *J. Am. Chem. Soc.* **2001**, *123*, 12775–12780.
(90) Paeng, I. R.; Nakamoto, K. *J. Am. Chem. Soc.* **1990**, *112*, 3289–3297.
(91) Fujii, H.; Kurahashi, T.; Tosha, T.; Yoshimura, T.; Kitagawa, T. *J. Inorg. Biochem.* **2006**, *100*, 533–541.
(92) Almond, M. J.; Crayston, J. A.; Downs, A. J.; Poliakoff, M.; Turner, J. J. *Inorg. Chem.* **1986**, *25*, 19–25.
(93) Bajdor, K.; Nakamoto, K.; Kanatomi, H.; Murase, I. *Inorg. Chim. Acta* **1984**, *82*, 207–210.
(94) Diemente, D.; Hoffman, B. M.; Basolo, F. *J. Chem. Soc., Chem. Commun.* **1970**, 467–468.
(95) Nakamoto, K.; Nonaka, Y.; Ishiguro, T.; Urban, M. W.; Suzuki, M.; Kozuka, M.; Nishida, Y.; Kida, S. *J. Am. Chem. Soc.* **1982**, *104*, 3386–3391.
(96) Shan, X. P.; Que, L. *Proc. Natl. Acad. Sci. U.S.A.* **2005**, *102*, 5340–5345.

(97) Bakac, A.; Scott, S. L.; Espenson, J. H.; Rodgers, K. R. *J. Am. Chem. Soc.* **1995**, *117*, 6483–6488.
(98) Spiro, T. G. In *Iron Porphyrins*; Lever, A. B. P., Gray, H. B., Eds.; Addison-Wesley: Reading, MA, 1983; Vol. 2, pp 89−159.
(99) Wagner, W. D.; Paeng, I. R.; Nakamoto, K. *J. Am. Chem. Soc.* **1988**, *110*, 5565–5567.
(100) Nakamura, A.; Tatsuno, Y.; Yamamoto, M.; Otsuka, S. *J. Am. Chem. Soc.* **1971**, *93*, 6052–6058.
(101) Horn, R. W.; Weissberger, E.; Collman, J. P. *Inorg. Chem.* **1970**, *9*, 2367–2371.
(102) Kryatov, S. V.; Chavez, F. A.; Reynolds, A. M.; Rybak-Akimova, E. V.; Que, L.; Tolman, W. B. *Inorg. Chem.* **2004**, *43*, 2141–2150.
(103) Bajdor, K.; Oshio, H.; Nakamoto, K. *J. Am. Chem. Soc.* **1984**, *106*, 7273–7274.
(104) Brunold, T. C.; Solomon, E. I. *J. Am. Chem. Soc.* **1999**, *121*, 8277–8287.
(105) Mizoguchi, T. J.; Lippard, S. J. *J. Am. Chem. Soc.* **1998**, *120*, 11022–11023.
(106) He, C.; Barrios, A. M.; Lee, D.; Kuzelka, J.; Davydov, R. M.; Lippard, S. J. *J. Am. Chem. Soc.* **2000**, *122*, 12683–12690.
(107) MacMurdo, V. L.; Zheng, H.; Que, L. *Inorg. Chem.* **2000**, *39*, 2254–2255.
(108) Momenteau, M.; Reed, C. A. *Chem. Rev.* **1994**, *94*, 659–698.
(109) Suzuki, M.; Ishiguro, T.; Kozuka, M.; Nakamoto, K. *Inorg. Chem.* **1981**, *20*, 1993–1996.
(110) Nakamoto, K.; Suzuki, M.; Ishiguro, T.; Kozuka, M.; Nishida, Y.; Kida, S. *Inorg. Chem.* **1980**, *19*, 2822–2824.
(111) Nakamoto, K.; Watanabe, T.; Ama, T.; Urban, M. W. *J. Am. Chem. Soc.* **1982**, *104*, 3744–3745.
(112) The shifts of 40−60 cm^{-1} can be identified for several peak combinations in the 760−1050 cm^{-1} range.
(113) Wang, L. P.; Wu, Q.; Van Voorhis, T. *Inorg. Chem.* **2010**, *49*, 4543–4553.